Synthesis, Characterization and Physical Properties of Nano-Antimony Oxyhalides

By

Nitasha Komal

A dissertation submitted in partial fulfillment of requirements for the

Degree of Master of Science in Chemistry

Supervised by

Dr. Zahida Malik

Department of Chemistry

School of Natural Sciences

National University of Sciences and Technology

Islamabad, Pakistan

2017

In the Name of Allah ,The most Compassionate and The most Merciful

Dedicated to,

My loving Grand Parents, Parents & Siblings

Acknowledgements

At first sight, I praise Allah, the almighty for providing me this opportunity and granting me the capability to proceed successfully. This thesis appears in its present form due to help and guidance of several people; therefore, I offer my sincere thanks to all of them.

I express my cordial thanks to my thesis advisor, ***Dr. Zahida Malik*** *for her encouragement, thoughtful guidance and critical comments. The door to her office was always open whenever I had queries about my experimental work or thesis write-up. She consistently allowed this thesis to be my own work, but steered me in the right direction.*

I am also thankful to the members of GEC; ***Dr. Ghulam Mustafa*** *and* ***Dr. M. Fahad Ehsan*** *for their constructive criticism and suggestions for improvement. I feel pleasure to pay a special thanks to the HoD Chemistry,* ***Prof Dr. Habib Nasir****, to the School of Natural Sciences (SNS) for financial support during my MS study. I greatly acknowledge the facilities and technical support provided by the other NUST schools like SCME and SMME.*

A precious thanks to my research fellows including ***Maryam Tahir, Samira Kanwal****,* ***Memoona Qammar*** *and other batch mates for their immense help during my research work. Last but not the least, I express my profound gratitude to my family for providing me support and continuous encouragement.*

Nitasha Komal

Abbreviations and Symbols

Sb_2O_3	Antimony Oxide
$SbCl_3$	Antimony trichloride
$Sb_4O_5Cl_2$	Antimony Oxy chloride
SEM	Scanning Electron Microscopy
XRPD	X-ray Powder Diffraction
IR	Infar red
Dia	Diameter
aq	Aqueous
l	Length
no	Number
DRS	Diffused Reflectance Spectroscopy
UV-Vis	Ultra Violet Visible
LCR	Inductance Capacitance and Resistance
DUT	Device Under Test
DFT	Density Functional Theory
PL	Photoluminescence
FWHM	Full Width at Half Maxima

Hz	Hertz
Rpm	Rate per Minute
eV	Electron Volt
WH	Williamson Hall
nm	Nanometer
Å	Angstrom
ε	Dielectric Constant
ε''	Dielectric loss
$tan\delta$	Tangent Loss
σ_{ac}	AC conductivity
$ln(F)$	Natural log of Frequency
PNC	Polymeric Nanocomposites
PVA	Poly vinyl alcohol

Abstract

The novel synthesis routes have been developed for the synthesis of nanorods and nanosheets of antimony oxychloride ($Sb_4O_5Cl_2$) in the dimension range of 55-90 nm by using single precursor. Nanostructures, microstructures and bulk single phase materials have been synthesized. X-ray powder diffraction analysis have confirmed the monoclinic crystal symmetry in space group $P2_1/c$ no.14 with structure type $Sb_4O_5Cl_2$ for the single phase nanorods, nanosheets, microstructures and the bulk materials. Rietveld refinement and the crystallite size investigations of the powder patterns revealed the lattice parameters and crystallite size increment in case of nanorods in comparison to the nanosheets. Through scanning electron microscopy, a composition near to the $Sb_4O_5Cl_2$ (at %) and the averaged dimensions; dia. ~ 50-90 nm, *l* ~ 2 μm for nanorods, dia. ~ 50-150 nm, *l* ~ 2 μm for nanosheets and thickness ~ 2-3 μm, *l* ~ 2 μm for microstructures have been observed. The PNCs have also been synthesized by using PVA as matrix with various compositions (1, 3 and 5 w/w%) of $Sb_4O_5Cl_2$ nanorods and -sheets. IR analysis has verified the PNCs synthesis in form of uniform films.

The optical properties of the nano and bulk materials have also been studied through DRS UV-Vis spectroscopy, the band gap widening has been observed while moving from bulk to nanoregime, *i.e.* 3.25, 3.31 and 3.34 eV, for bulk, nanosheets, and nanorods, respectively due to quantum confinement. In the case of nanosheets, highest value of dielectric constant has been observed, *i.e.* 87, as compared to nanorods 40 and the bulk 35.5, respectively. The nanosheets have also shown the highest value of dielectric and tangent loss with increase in frequency due to the least crystallite

size of this material. Nanosheets have depicted the higher AC conductivity at low frequency due to the alignment of the charges but its value decreases at the higher frequency due to lack of time for alignment of the charges. However, nanorods and bulk material had no change throughout the frequency range. The hopping phenomenon has been observed in all three cases with most prominent one in bulk case at higher frequencies.

Table of Contents

List of Tables

List of Figures

Chapter 1

Introduction

1.1Nanoscience and Nanotechnology

The concept of "Nanoscience" was first time given by an American physicist Richard Feynman in 1959. According to him "*There's plenty of room at bottom*" [1]. Afterwards, many researchers have explored and contributed in the development of this field. Mainly, the study of structure and properties of the materials in nano range is called *Nanoscience*. While the fabrication of materials and devices having at least one dimension in 1-100 nm range, is described as *Nanotechnology*. There are certain physical and chemical properties which vary dramatically as we move from bulk to nanoregime e.g. chemical reactivity, optical, electrical, mechanical, photocatalytic and magnetic properties. The basis behind this dramatic change in properties is large surface area and the quantum confinement effect. The astonishing and useful properties of these materials make them the potential candidate for various device applications.

Two main approaches; bottom up approach and top down are mainly employed for the synthesis of nanomaterials. Bottom up approach is utilized by nano-chemist to build nanomaterial via self-assembly of atoms or progressing from small or subordinate units to larger units which mainly includes the wet chemical synthesis. On the other hand, nano-physicist employs top down strategy by breaking/milling the larger piece of materials to get the nanomaterials [2]. As nanomaterials have imparted role in every field of science

and technology by improving or even revolutionizing many industries like biomedical, pharmaceutical, agriculture, communication, and electronics [3-5].

1.2 Classification of Nanomaterials

Nanomaterials are generally classified into four main classes based on dimensions.

(a) Quantum dot (0-Dimensional)
(b) Quantum wire (1-Dimensional)
(c) Quantum well (2-Dimensional)
(d) Nanocrystals or Nanoclusters (3-Dimensional)

1.2.1 Quantum dot (0-D)

When all the dimensions of nanostructures lie in 1-100 nm or the motion of the electron is confined in all dimensions, it is called quantum dot e.g. nanoparticles and nanospheres.

1.2.2 Quantum Wire (1-D)

When materials have two out of three dimensions lying in nanometer regime or the motion of electrons is confined in two dimensions, it is known as the quantum wire. These are also known as 1D nanostructure including nanorod, nanowire and nanofilms.

1.2.3 Quantum Well (2-D)

These are the nanostructures in which only one out of three dimensions lies in nano scale- also known as 2D nanomaterials. The quasi-electrons can easily move in two dimensions while their motion is restricted in one dimension e.g. nanotubes, nanoplates and nanosheets are some examples of the quantum well.

1.2.4 Nano-crystal or nanoclusters (3-D)

These are 3D nanomaterials usually do not have any dimension in nanoregime but are made up of clusters of nanotube, nanowires or nanoparticles therefore, they are called 3D nanomaterials.

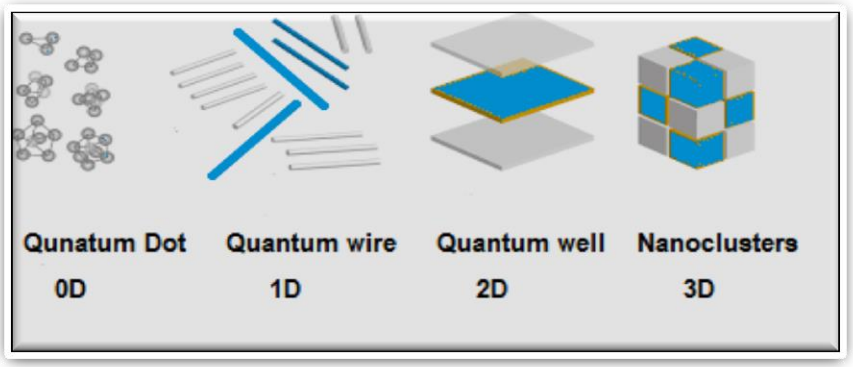

Figure 1.1: Classification of nanomaterial based on dimensions

1.3 Nanocomposites

The composites mainly have two phases; reinforcing and the matrix phase while in case of nanocomposites one should be in nano-range [6]. There are various reports on nanocomposites [7] but above all the polymeric nanocomposites are the multiphase products in which the nanomaterials (1D, 2D or 3D) act as reinforcing phase while matrix phase is made up of polymers.

For the past few decades, polymeric nanocomposites have been extensively studied as a class of materials for variety of applications including enhanced; gas barrier performance, thermal, mechanical and flam retarding properties. The nanofibres, hollow nanofibres, core–shell nanofibres and nanorods/nanotubes have a great potential for polymer based composites with the broad range applications including; homogeneous and heterogeneous catalysis, sensors, filter applications, environmental applications, food packging, industrial application, optoelectronics etc [8-10]. Different PNCs of PVA

(poly vinyl alcohol), PP (polypropylene) and polymer-clay nanocomposites have been synthesized and explored to observe the thermal stability with improved flame retardancy [11-13].

1.4 Applications of Nanotechnology

Thorough studies have proved the nanotechnology as a guide for synthesis and fabrication of nanomaterials for the most advanced applications. Some of the applications of nanotechnology are summarized in this section.

1.4.1 Energy Sector

Energy is contemplated as a life line of any economy and most integral instrument of socioeconomic growth of a country. Energy crisis is a highlighting issue of the global world. Increasing energy demand and depleting non-renewable energy require the production of novel energy resources or reclaimed the waste heat. Fuel cells, hydrogen combustion via nano catalyst, photovoltaics cells, solar cells, lithium storage batteries and most important thermoelectric nanostructures are blessings of nanotechnology [14-16].

1.4.2 Water Purification and Waste Water Treatment

Potable and affordable water that is free of toxic components is a vital requirement of human health but it is a formidable challenge of this century to fulfill this demand of human beings. Nanotechnology is contributing a crucial role to cope with the needs of clean water. It has enabled water and wastewater treatment promises not only to overcome major challenges faced by existing treatment technologies, but also to provide new treatment capabilities that would allow economic utilization of unconventional water sources to expand its supply. Some waste or toxic components of water can be removed via nano-adsorbents. Metal oxides adsorbents such as iron oxide, titanium dioxide and alumina are effective and low-cost adsorbents for removal of heavy metals from water.

Moreover, nanostructured membranes of carbon nanotubes, silica and cellulose-based materials, functionalized with amino acid homopolymers have also been employed in water treatment against microorganism (viruses, bacteria, etc) and toxic metal ions [17, 18].

1.4.3 Textile Industry

Out of the many other applications of nanotechnology, the textile industry has been recently added as one of the most assisted and profitable sector. Various nanomaterials e.g. nanofibres/carbon nanocomposite, nanoparticles of silver (Ag), titanium dioxide (TiO_2) and zinc oxide (ZnO) have been manipulated in the textile industry to improve the durability, fire retardancy and comfort. Because of low production cost, UV-blocking ability, and antimicrobial activity, nanotechnology has been proven as a potential applicant in electronic textile, composite fabric and material, military combat garments, climate control wears and protective clothing [19, 20].

1.4.4 Pharmaceutical and Biomedical

Nanotechnology has also gained the focus of pharmacist and biomedical researchers because of its effectiveness. Currently it has been employed in diagnostic devices, analytical tools, antimicrobial agents and detection tool for pathogens. It plays a significant role as drug delivery vehicle, gene therapy, and organ transplantation. Furthermore, new nanomaterials have been designed that can act as anticancer agent with the ability to target the specific cancerous cells [21, 22].

1.4.5 Electronics

Electronic industry is also enjoying the miracles of nanotechnology as it has contributed its share in electronic devices like Data Memory, Displays, Laser Diodes, Glass Fibers and Conductive Coatings. Semiconductor nanocrystals, graphene and di-metal

chalcogenides have employed in various electronic devices. Small size, better efficiency, high surface to volume ratio and light in weight: these properties make them better choice in different electronic devices [23, 24]. Beside these applications of nanomaterials, nanotechnology has its utilization in cosmetics and sunscreens, household items, automotive industry and sports items.

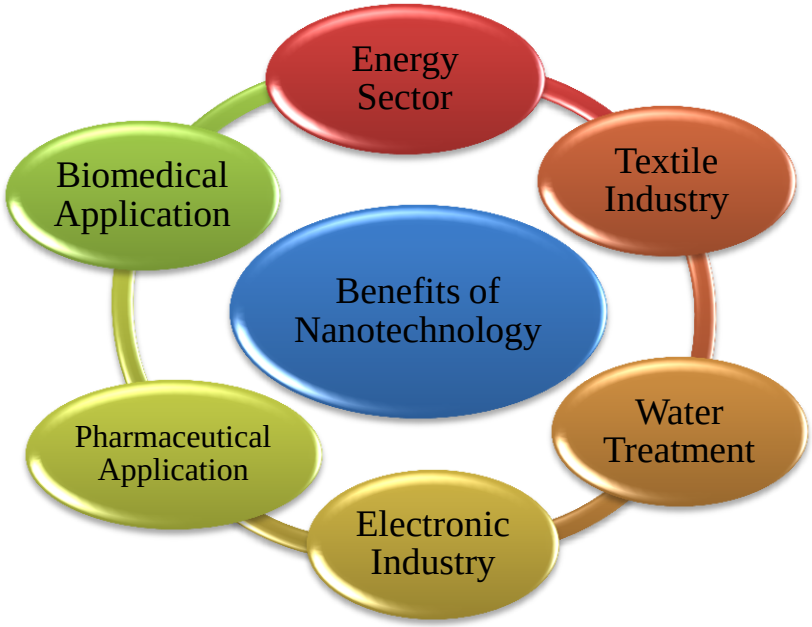

Figure 1.2: Applications of nanotechnology in various fields

1.5 Characterization Techniques

The morphology, structure, composition, size and properties of prepared samples have been studied by using different techniques. The brief description on principle and instrumentation has been given in the next section:

1.5.1 Scanning Electron Microscopy (SEM)

In 1938, Manfred von Ardenne invented the *Scanning Electron Microscopy* [25]. It is a versatile and specialized microscope that uses electron beam to determine the surface morphology and composition of the material under investigation. The non-conducting sample should be coated with a layer of some conducting material. Usually, the coating material include; carbon, gold and aluminum. Generally, SEM involves an optical system to attain an electron probe, a sample stage to place the sample, a secondary electron detector to gather the coming secondary electrons, an image display system and the operating system to operate all the functions [26, 27]. The general construction of SEM is given below;

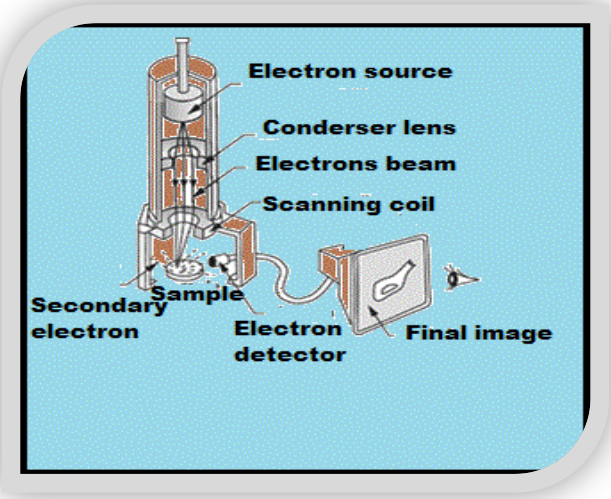

Figure 1.3: Pictorial representations of main parts of SEM

(a) Electron Source

An electron gun produces thermo-electrons by heating the tungsten filament (cathode). These electrons are then gathered on a metal plate (anode) in a form of beam. The speed of electron emission is controlled by adjusting the accelerating voltage 1-30 keV.

Figure 1.4: Scanning Electron Microscope

(b) Condenser and Objective lenses

The microscope utilizes an electromagnetic lens to adjust the diameter of the electron beam. When an electric current passes through a wire

coiled around an iron cylinder, a symmetrical magnetic field is developed. This magnetic field then affects the electron beam. Two different types of lenses named as condenser and objective are used in an electron microscope, present below the electron gun .The main function of both lenses is to focus and to control the diameter of an electron beam that falls on the sample.

(c) Sample stage

The samples are studied at high resolution via SEM, therefore, the sample stage should move smoothly and stay stable that can support the sample. The sample stage can move along X and Y axis (horizontal movements), Z movements (vertical), sample tilting (T) and R used for rotation. Basically, these movements are employed for selecting the specific area, resolution and depth focus.

(d) Secondary electron detector

The incident beam electrons ionize the sample atoms by knocking out the outer shell electrons. The secondary imaging mode is given by the secondary electrons, which provides information about the surface topography of material under observation. A detector is used as secondary electron detector which needs voltage about 10 keV. It attracts the secondary electrons coming from the sample. These electrons produce light as they collide with fluorescent material. This light is directed towards the photomultiplier tube to amplify the light signal. Then this light signal is again converted as amplified electric signals which are then collected by collector placed next to it.

(e) Display Unit

An output signal from the detector is then amplified and transferred to display unit that is a liquid crystal display. The scan speed changes in steps, a fast scan is used for observation and slow scan rate is used for acquisition to save the images of various areas.

1.5.2 X-Ray Diffraction

X-Ray diffraction is an important analytical tool for qualitative and quantitative analysis of crystalline materials. It provides a way to study the phase distribution, degree of crystallinity, crystallite size, epitaxy, geometry and lattice parameters etc [28].

Basic principle behind X-ray diffraction technique is the constructive interference of the X-ray radiation diffracted by the crystalline materials, thoroughly explained by Bragg's Law. According to which an X-ray reflected from the surface of a substance, travels less distance than an X-ray which reflects from a plane of atoms inside the crystal. The penetrating X-ray travels down to the internal layer, reflects, and travels back over the same distance before coming back at the surface. The distance travelled depends on the separation of the layers and the angle at which the X-ray entered the material. Diffraction occurs only when the distance travelled by the parallel X-rays are an integer multiple of the wavelength. Bragg expressed it in equation known as Bragg's Law as mentioned below,

$$n\lambda = 2dSin\theta$$

Where n is an integer whose value is whole number for constructive interference, λ is a wavelength of the incident radiation, θ is an angle between the incident ray and layers of crystal while d is the interspacing between the layers.

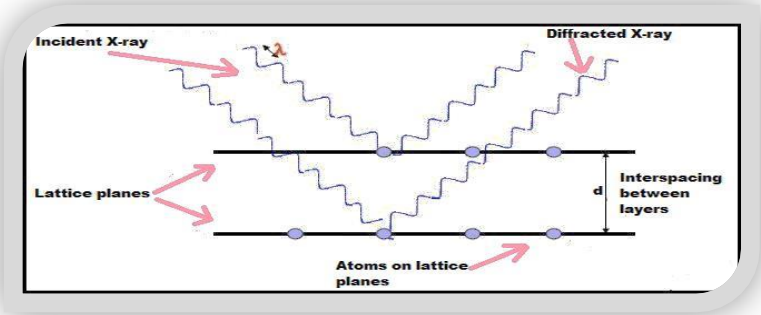

Figure: 1.5: X-Ray Diffraction

Basically, in XRD, a monochromatic X-ray radiation beam is focused on sample material to determine the structural information of the crystal lattice. Most of the time, the material is crystalline in nature with repeating patterns. Typically, polychromatic X-rays are produced in cathode-ray tube (CRT). The polychromatic X-rays pass through a monchromator that acts as a filter and produce monochromatic X-rays which hit onto the material atomic planes, separating the diffracted, transmitted and absorbed rays. Application of 15-60 kV current within the tube gives electrons which hit a Cr, Fe, Co, Cu, Mo or Ag anode from which X-ray beams are generated. Thus, produced X-rays are then collimated and directed onto the sample. Various phenomena take place upon interaction of radiation and sample e.g diffraction, transmittance, refraction, scattering and some of the x-rays have absorbed by the sample. These rays are used to generate the spectra containing various peaks.

For qualitative analysis POWDER CELL program has been used [29] while quantitative Rietveld refinements of the X-ray powder diffraction data were performed with the FULLPROF program in FullProf Suite [30]. The drawback of this conventional *powder* method was that the diffraction peaks grossly overlap, thereby preventing the proper structure determination. *The "Rietveld Method" creates a virtual separation of these*

overlapping peaks, thereby allowing the accurate determination of the structure. This *quantitative phase analysis* method has been so successful that nowadays the structure of materials, in the form of powders, are routinely being determined which are near to the single crystal analysis in accuracy [31]. The principle of Rietveld refinements is,

Calculated intensity at point i of the diagram,

$$Y_{ic} = Y_{ib} + \sum_{\emptyset} S_{\emptyset} \sum_{k} G_{\emptyset}(2\theta_i - 2\theta_{k)} I_k$$

G__ normalized profile shape function

I___ intensity of the k^{th} reflection

S___scale factor of phase ϕ Summation performed over all phases ϕ, and over all reflections k contributing to the respective point.

y_{ib}__background

Intensity of Bragg reflections,

$$I_k = m_k L_k \ |F_k|^2 \ P_k \ A_k$$

Where,

m_k___multiplicity of k^{th} reflection

L_k____Lorentz-polarization factor

$|F_k|^2$__structure factor

P_k____preferred orientation factor

A_k___absorption factor

The main goal is to minimize the residual function,

$$\sum_i w_i \ (Y_i^{obs} - Y_i^{cal})^2$$

Where,

$w_i = 1/y_i^{obs}$

y_i^{obs}___ observed intensity at the i^{th} step

y_i^{calc}___ calculated intensity at the i^{th} step

1.5.3 Infar Red Spectroscopy

IR spectroscopy is an analytical technique to analyze the material specifically organic compounds in solution and the solid films form. The compounds with the certain values of dipole moment are IR active. Usually IR radiations having wavenumber range of 4000 - 400 cm^{-1} (wavelength 2.5 μm to 15 μm) are employed for this analysis. When the sample is irradiated with IR radiations, electrons absorb energy and undergo excitation from lower to higher vibrational energy levels. The excited electron undergoes de-excitation resulting in emission of photon of characteristic wavelength The energy of emitted photons is calculated and spectra are obtained in form of wavenumber vs absorbance or transmittance [32].

1.5.4 UV-Vis Diffused Reflectance Spectroscopy

Figure 1.6: UV-VIS DRS

UV-Vis diffuse reflectance Spectroscopy (DRS) is an analytical tool to measure optical properties of the solid powder. The basic principle behind UV-Vis spectroscopy and UV-Vis DRS is the same. In both techniques electronic transition take place by absorption of visible light having energy greater than the band gap energy between a conduction band

and a valance band. In UV-Vis spectroscopy a relative change in transmittance from the sample solution is measured while in UV-Vis DRS, relative change in reflectance from the sample is considered. The spectral range of UV-Vis DR lies in range 50,000-5000 cm^{-1}. UV-Vis DRS is usually employed for investigating optical property like band gap and color variation [33].

1.5.5 LCR Meter

It is an electronic instrument employed to calculate capacitance, inductance and resistance of the material under observation with high precision and accuracy.

Figure 1.7: LCR Meter

The name LCR is an abbreviation of inductance, capacitance and resistance denoted by symbols L, C and R, respectively. Capacitance is the quantity of charge that a capacitor can stored at given voltage and its unit is Faraday. While inductance is the characteristics of a coiled wire to oppose any change in electric current flowing through it and is measured in Henry. Whereas resistance is the property of material to resist the movement of electron or electric current passing through, it is commonly measured in Ohm (Ω). LCR meter also provides value of dissipation factor and quality factor. Moreover the value of current and voltage can also be calculated by this electronic device. The quantity measured by LCR meter is impedance that is actually resistance of alternating and direct current. This impedance is a vector quantity depending upon two scalar entities named as resistance and reactance. Basically, reactance is the resistance of alternating current due to combined effect of inductance and capacitance.

1.5.5.1 Techniques used in LCR meter

Commonly two approaches have used in LCR meter.

(a) Bridge Technique

The bridge technique is only applicable for studies at low frequency *i.e*. below 100 kHz**.** This approach is based on Wheatstone bridge principle in which the device under test (DUT) is placed in it and its impedance is denoted by R_U (unknown impedance). The other impedances R_3 and R_4 are known. The value of Impedance R_1 varies until the flow of current stops in a device. At this balance position, the impedance of unknown can be calculated by employing the equation given below [34].

$$R_1/R_U = R_3/R_4$$

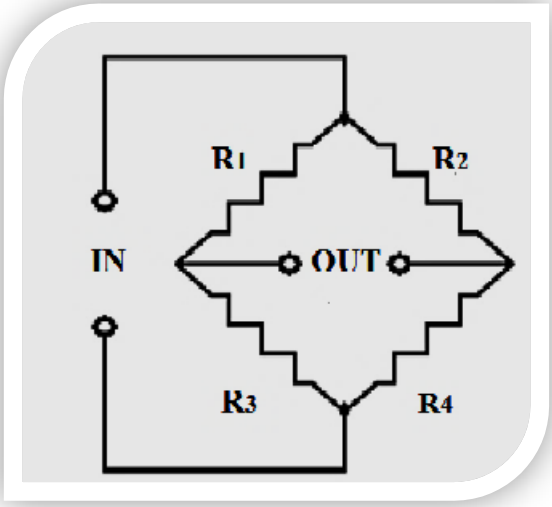

Figure 1.8: Circuit diagram for bridge technique of LCR meter

(b) Current Voltage Method

This approach can be used for studies at higher frequencies. It finds the value of current and voltage first which are then used for calculation of impedance of the device under test [35].

1.6 Aims and Motivations

It has been observed that there are extensive reports on the shape, size, morphology and microstructure dependent properties of nanomaterials. Antimony-based materials; mainly the oxychloride have attracted great attention because of their astonishing properties like high photocatalytic catalytic activity [36], superior flame retardancy [37] and applications in energy storage devices and gas sensors [38]. No doubt they exhibit fascinating properties but a few studies have been carried out for the synthesis of such nanomaterials. There was a need to develop a facile and economical route for the synthesis of nano-antimony oxychloride and investigation of their properties.

Antimony oxychloride will be proved as one of the most significant nanomaterials in upcoming research and requisites due to the ease of production method, non-hazardous nature and scale ability.

The key goal of this research is the synthesis of bulk and nano-antimony oxychlorides via simple wet chemical approach. Then to optimize the various reaction conditions to control the morphology and size of different nanostructures. After this optimization the optical and electrical properties of nano-antimony oxychloride will be explored in comparison with those the bulk counterpart.

Chapter 2

Literature Review

2.1 Compounds of Antimony

Antimony is semimetal in nature because of its properties intermediate properties between non-metals and metals. Antimony is similar to arsenic and bismuth usually forms its oxides, halides, hydrides and hydroxides with the capability to react further with other compounds.

2.1.1 Oxide of Antimony

Antimony usually exists as Sb_2O_3 while sometimes it forms Sb_2O_5 having +3 and +5 oxidation states. Antimony oxide is almost insoluble in water while it can react with acid and alkalis. The oxide of antimony has been synthesized via following reactions,

$$2Sb_2S_3 + 9O_2 \longrightarrow 2Sb_2O_3 + 6SO_2$$

$$4Sb + 3O_2 \longrightarrow 2Sb_2O_3$$

2.1.2 Chlorides of Antimony

Two chlorides of antimony *i.e.* $SbCl_3$ (+3) and $SbCl_5$ (+5) exist in nature, out of which antimony trichloride is more common. Antimony trichloride has been prepared via the following reaction given below

$$2Sb + 5Cl_2 \longrightarrow 2SbCl_5$$

$$2Sb + conc.6HCl \longrightarrow 2SbCl_3 + 3H_2$$

2.2 Properties of Antimony Oxide

Sb_2O_3 lies in family of p-type semiconductors having indirect and wide band gap (~3.3 eV). Various aspects of study and the published work state that their properties vary while moving from bulk to nanomorphology. Antimony oxide nanomaterials have been investigated widely owing to their optical, electronic, surface wettability, photocatalysis, flame retardancy, optoelectronic and electrochemical properties. These properties make them better contestant for commercially available optoelectronic nanodevices.

2.2.1 Crystal Structure

For the 1st time in 1938, Buerger & Hendricks have investigated the crystal structure of antimony oxide. They have calculated the values of fractional coordinates of orthorhombic Sb_2O_3 [39]. Afterward, Christer Svensson in 1974 has reinvestigated the crystal structure of antimony oxide and found it closely related to already reported results. Recent electronic studies via DFT (density functional theory) show that Sb_2O_3 exists in three different polymorphic forms and isomorphs to As_2O_3 in the virtual view. α-Sb_2O_3 has been investigated widely due to its thermodynamic stability. α-Sb_2O_3 (senarmontite), is present in form of cubic unit cell with lattice parameter a = 11.1519 Å and in $Fd\bar{3}m$ space group. A detailed study revealed that each unit cell constitutes Sb_4O_6 molecular units and each Sb atom is bonded to 3 oxygen atoms while each oxygen atom is attached to two Sb atoms in bent angle form These Oxygen atoms give the base of tetrahedron with forth vertex far from cluster vacant [40, 41]. The bond angles between Sb-O having different coordination given in table 2.1 given below.

Table 2.1 The bond angles among Sb-O in Sb_4O_6 molecular units [40]

Atoms	**Bond Angles (^{o})**
O^I-Sb^I-O^I	95.9(2)
O^I-Sb^I-O^{II}	160.8(5)

O^{I}-Sb^{I}-O^{II}	71.6(2)
Sb^{I}-O^{I}–Sb^{I}	132.4(2)

2.2.2. Optical properties

Optical properties play a key role in determining the applications of material in solar panels, photo-detector and other photo-electronic devices. UV-Vis and PL spectroscopy are the most convenient techniques used for the measurement of optical properties. A purposeful thorough study on optical properties of Sb_2O_3 has been carried out by various groups via UV-Vis spectroscopy. According to these investigations, optical properties also deviate by changing the morphology and composition of nanomaterials. The detailed studies of UV-Vis spectra exhibit that various nanostructures of Sb_2O_3 show a broad absorption band in range of 360-380 nm and lie in visible range of spectrum, depicting band gap range in 3.2-3.5 eV [42-45].

2.2.3 Photoluminescence

PL (Photoluminescence) spectroscopy is used as a key tool for calculating the light emitting property. Diverse forms of Sb_2O_3 nanostructures have shown dominating light emitting property. Comprehensive studies have been carried out to measure the PL in antimony trioxide nanomaterials. Similar to the optical properties, PL is also size and morphology dependent. Numerous groups of researchers have found the PL spectra of antimony trioxide nanostructures under different conditions. With respect to their calculations, antimony trioxide nanostructures give a broad emission peak in range of 370-380 nm which corresponds to the 3.25-3.4 eV band gap range. PL spectra also gives information about vacancies related defects produced as a result of oxygen removal [42, 44, 46-48].

The superior optical, photoluminescent, high refractive index and great abrasive resistance made antimony oxide a good candidate in lenses and other optical nanodevices.

2.2.4 Flame Retardancy

Sb_2O_3 nanomaterial has also been employed in polymer industry as flame retardant. It becomes very handy flame retardant when it is used in combination with halogenated resins or polymer. F. Lie et al. in 2007 have elucidated the flame retardancy of Sb_2O_3 nanoparticles. TGA (thermo gravimetric analysis) has been employed as a verification technique for calculation of flame retardant behavior. According to their observation, the flame resistance property of resins was extended by the addition of antimony trioxide nanoparticles [49].

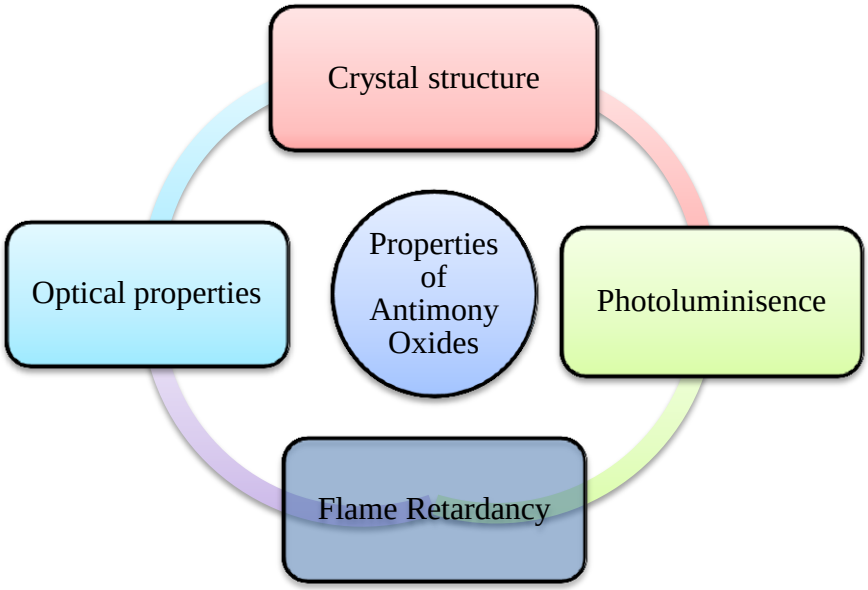

Figure 2.1: Important Properties of Antimony Oxides

2.3 Synthesis and properties of Antimony oxyhalides

In literature, Antimony Oxyhalides including SbOX (X = F, Cl, Br and I) and BiOX (X = F, Cl, Br & I) have communicated. Few investigations have also been reported on synthesis of single crystal and properties of antimony oxyhalides.

2.3.1 Crystal Structure of Antimony Oxyhalides

Crystal structure of antimony oxyhalides $Sb_aO_bX_c$ (X = F, Cl and Br) with various compositions have been reported in the literature. Four different forms of SbOF have been reported [50], the L and M form of SbOF were stable, existing in orthorhombic form while H-SbOF exists in cubic geometry. The single crystal of L and M form of SbOF has been synthesized and studies by A. Astrome in 1972 and 1973 [50, 51]. According to this study, the M form of SbOF has orthorhombic geometry and the space group $Pbca$ with the lattice parameters; a = 11.673, b = 5.587 and c = 12.267 Å [51]. Moreover, he has also elaborated the structure of L-SbOF in 1973. Similar to M form of antimony oxyflouride, L-SbOF also has orthorhombic geometry in space group $pmna$ with lattice parameters; a = 8.873, b = 4.099 and c = 5.483 Å [50].

Specifically, the crystal structure of antimony oxychloride has calculated in detail; $Sb_4O_5Cl_2$ has been reported first time by M. Edstrand with monoclinic symmetry (space group $P2_1/C$ a = 6.229, b = 5.107 c = 13.5 Å and β = 97.27º) [52]. Reinvestigation of the same structure has been reported [53] with the major difference in Sb-O distances. Recently, single crystal of $Sb_4O_5Cl_2$ has been synthesized via hydrothermal route by using the $SbCl_3$ and HCl in aqueous medium [54]. A new structure, Sb_3O_4Cl has been prepared hydrothermally in monoclinic geometry (space group $P2_1/C$, lattice parameters; a = 9.6351, b = 5.3059, c = 5.9851 Å and β = 94.745º) [55] by using $SbCl_3$ and $VOCl_2$ precursors. Other Oxyhalides, including SbOF, SbOCl [50, 51] and $Sb_8O_{11}X_2$ (X=Cl, Br)

[56] have also been reported. The crystallographic parameters of these two structures are provided in table given below,

Table 2.2 Crystallographic data for $Sb_8O_{11}X_2$ (X=Cl and Br), in Space group P-1 [56]

Compound	Lattice Parameters	
	(Å)	(^{o})
$Sb_8O_{11}Cl_2$	a = 10.317(2) b = 11.269(2) c = 13.939(3)	α = 79.29(2) β = 76.29(2) γ = 73.00(2)
$Sb_8O_{11}Br_2$	a = 10.4875(6) b = 11.3375(7) c = 13.9831(9)	α = 79.430(5) β = 76.471(6) γ = 73.061(5)

2.3.2 Synthesis of Antimony Oxychloride Micro and Nanostructures

Up till now, various nanostructures of antimony oxychloride with different morphologies have been prepared via solid state and wet chemical route. In recent past, The $Sb_8O_{11}Cl_2(H_2O)_6$ needle-like microstructures have been reported by Li et al. They have prepared microstructures with dimensions (diameter = 2 μm and length<20 μm) [57].

In 2007 Zheng Bo et al. has been synthesized Antimony oxychloride ($(Sb_4O_5Cl_2)$ has via electrochemical method by using Sb as anode, different conducting metals as cathode and chloride salt dissolved in HCl employed as electrode [58]. In the very next year, X. Y. Chen has investigated the synthesis of nanocrystals ($Sb_4O_5Cl_2$ and $Sb_8O_{11}Cl_2$) by hydrothermal approach with $SbCl_3$, NaOH and ethylene glycol as precursors. The reaction was carried out at 120^o C for 12 h in Teflon lined autoclave. The prepared materials were filtered, washed with distilled water and ethanol and vacuum dried at 60^o C. They have obtained nanowires of $Sb_8O_{11}Cl_2$ having dimensions diameter = 50 nm and length up to 10 μm [59]. In 2009, hydrothermal synthesis of ID nanostructures of antimony oxychloride has been reported by using $SbCl_3$, ethanol and sodium hydroxide precursors in aqueous medium. The lacteous colloidal suspension of antimony trichloride was poured into Teflon lined autoclave maintained at 180^{o}C for 2-20 h. They

have also studied the effect of reaction time over the morphology of nanowires. According to them, as the reaction time increases from 2 to 20 h the morphology of nanowires varies from irregular nanowire bundles (dia. = 60-110 nm and l = 2-5 μm) to the uniformly self-oriented nanowires with dimensions; dia. = 100-130 nm and l ~ 10 μm [60]. Later on J. Zhou et al. has reported the synthesis of sheaf-like microcrystals of antimony oxychloride ($Sb_8O_{11}Cl_2(H_2O)_6$). They have used $SbCl_3$, ethylene glycol, PVP (poly-vinylpyrrolidone) and NaOH. A solution of $SbCl_3$ was prepared in ethylene glycol under constant stirring. Then aq NaOH solution was added dropwise to maintain pH. After vigorous stirring for 5 h, the white precipitates of antimony oxychloride were obtained. The precipitates were filtered, washed and vacuum dried at 50^o C. They have reported the particle size of l = 3-4 μm and dia = 270 nm obtained from SEM [61]. In the same year, Y. J. Zheng et al. has been prepared highly pure (99.50 %) antimony oxychloride from high-arsenic refined bismuth dust in a process of hydrochloric acid leaching [62]. Recently, hollow microspheres of $Sb_4O_5Cl_2$ have been reported via pH-regulated template free method. They have used $SbCl_3$ as precursor, solvents (ethyl alcohol and water) and ammonia as pH stabilizers. By changing the pH of solution they have prepared different nanostructures with diameter of several hundred nanometers and length in microns [63]. During last half decade, different groups of researchers have investigated the synthesis of $Sb_4O_5Cl_2$ composites with various compounds. In 2014, P. Li et al. has reported the synthesis of $PbCl_2/Sb_4O_5Cl_2$ composite via simple solution route. The prepared particles have size range of about 50-100 nm. They have also compared its electrochemical behavior of the composite with $PbSO_2Cl$ [64]. In the upcoming year, hydrothermal synthesis of three dimensional spherical microcrystals of $Sb_2S_3/Sb_4O_5Cl_2$ has been reported by [65]. In the same year, Y. Liu et al. have explored the synthesis of g-C_3N_4–$Sb_2S_3/Sb_4O_5Cl_2$ by hydrothermal route [36].

No doubt these methods give good yield of halogenated antimony oxides but at least one solvent is a must need for the shape and size control. Moreover these techniques are

tricky and time taking. Up to our knowledge, this is the 1st study that investigates the synthesis of two different nanostructures of antimony oxychloride via facile precipitation method with a sole precursor. Moreover this work also includes the synthesis of polymer based nanocomposites of antimony oxychloride nanostructures. The convenient handling and utilization of single precursor is the key point of this study, without the use of any organic or inorganic solvents. We report here the most facile synthesis/control of ID nanorods and nanosheets along with the comparison of their optical and dielectric properties with that of the bulk.

2.4 Applications of Antimony Oxychloride

Up till now, it has been studied that nanostructures have proved to be very efficient materials in various optical, electronic and energy production as well as storage devices. Specifically nanostructures of antimony oxychloride have been thoroughly studied because of their diverse applications. Different compounds of Antimony oxychlorides including (SbOCl, $Sb_4O_5Cl_2$, $Sb_8O_{11}Cl_2$) exhibit a remarkable flame retardant properties which can not only be used as a flame retardant alone, but can also give better synergistic effects when employed in combination with a halogenated organic compounds [66]. Sb-based oxide and oxychloride materials have also attracted attention due to their better efficiency in energy storage devices [67]. As $Sb_4O_5Cl_2$ is semiconductor in nature. The photocatalytic activity of $Sb_4O_5Cl_2$ composites has been reported. It has not only uses as a photocatalyst alone but can be coupled with photocatalyst to improve their photocatalytic activity for degradation of methyl orange [68, 36].

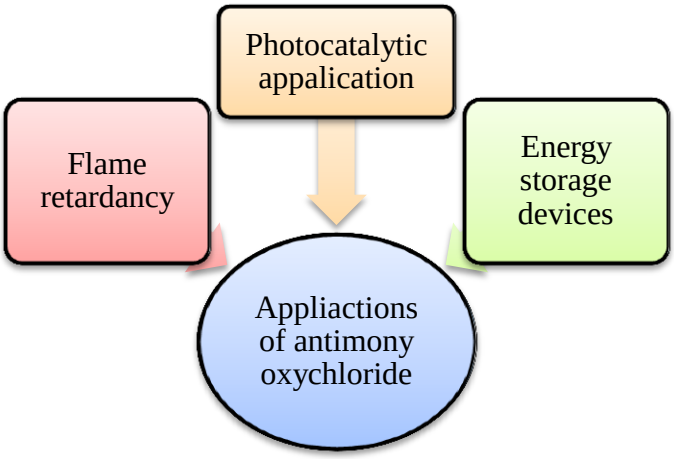

Figure 2.2: Major applications of Antimony oxychloride

Chapter 3

Experimental & Characterization Techniques

3.1 Experimental

This chapter includes the synthesis of bulk and nanomaterials of ternary antimony oxychlorides.

3.2 Synthesis of Bulk and Nanostructures-$Sb_4O_5Cl_2$

A feasible wet chemical approach has applied for the preparation of well-defined bulk and nanostructures of antimony oxychloride. The wet chemical strategy is very advantageous as compared to solid state approach as it is simple, environment-friendly, economical and easy to handle. The list of reagents and precursor used are given below,

Table 3.1 List of chemicals and reagents used in synthesis

Chemicals and Reagents	**Molecular weight *(amu)***	**Purity *(%)***	**Company**
Antimony (III) Chloride	228.26	99	BDH
Sodium hydroxide	40	99	-
Acetone	46	99.5	AR

3.2.1 Synthesis of Bulk material

A distinct room temperature synthesis of antimony oxychloride via solubility difference method has been developed in this study. We first dissolved the precursor in the solvent then add another solvent which has negligible solubility of precursor in it. The final product was separated by filtration, washing and finally drying was carried out to remove solvent. Antimony trichloride was used as source of antimony while sodium hydroxide has employed as a structure directing agent. In the typical synthesis, 0.456 g (2 mM) of antimony trichloride was added in a flask containing 10ml of acetone. The solution was stirred until the salt is completely dissolved in it and a clear transparent solution was obtained. In the next step, 10 ml of dist. water was added in flask, as a result white color gel was formed. Afterwards 8-10 drops of aq 6 M NaOH were added into the flask, resulting solution was stirred and covered with aluminum foil and was placed static for five days. The whole reaction carried was out at room temperature. After 5 days, white colored transparent large crystals were obtained. The crystalline material was separated by filtration followed by washing (4-5 times) with distilled water to remove unreacted precursor. At the end, the material was vacuum dried at 70o C for 2 h and sample was further used for characterization.

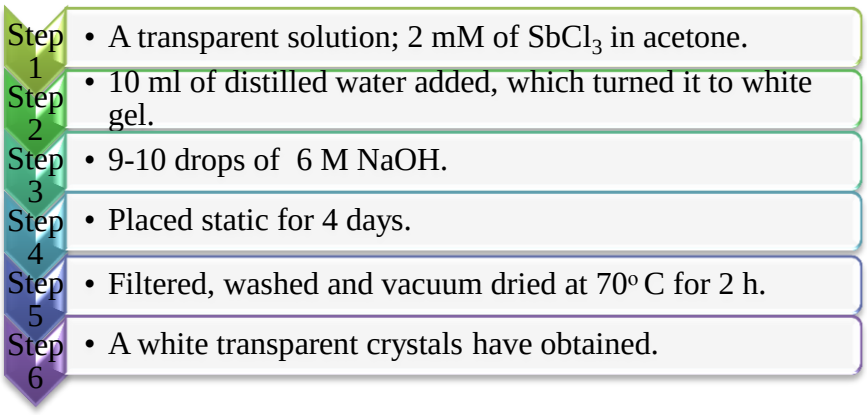

Figure 3.1: Graphical presentation of synthesis of bulk antimony oxychloride

3.2.2 Synthesis of Nano Antimony Oxyhalides

In this work, *Nano-Antimony Oxychloride has been prepared* with various morphologies and dimensions via precipitation method. This method is based upon the precipitation of nano-sized particles within solvent. The inorganic metal salt, such as chloride, nitride etc. is dissolved in the solvent to form hydrates for example, Al $(H_2O)_3$+ or Fe$(H_2O)_3$+. These hydrates are added with basic solutions, such as NaOH or NH_4OH. The hydrolyzed species precipitate out and then filtered, washed to remove byproduct followed by drying and calcined in order to get the final product [69].

By optimizing the conditions, antimony oxychloride nanostructures have been synthesized via simple precipitation method. To prepare the nanostructures, we have carried out the hydrolysis of antimony (III) trichloride ($SbCl_3$) have been carried out with three different amounts *(0.0228 g (1 mM), 0.456 g (2 mM) & 0.684 g (3 mM)* and added to 20 ml of distilled water and the resulting solutions were heated for 30 min at 60º C. The white precipitates thus obtained were filtered, washed with distilled water and dried in vacuum oven at 70^o C for about 2 h. The sample with 2mM concentration of $SbCl_3$ has been selected for further experimentation because the particles obtained had refined geometry and good yield. In order to control the size reduction, an another sample of antimony oxychloride was prepared by hydrolyzing (*2 mM)* solution of $SbCl_3$ in ultrasonic bath, maintained at 60º C for about 1 h. This resulted in the formation of white microcrystals of antimony oxychloride after separation through filtration, washing with distilled water and drying in vacuum oven at 70^o C for 2 h.

To further reduce the size from micro to nano-regime, the reaction materials have been ultrasonicated for longer time interval. The white powder of antimony oxychloride nanomaterials was obtained by ultrasonication of (*2 mM)* aqueous solution of antimony (III) trichloride ($SbCl_3$) for about 2.5 h at 45º C. Afterward, the solution with precipitates was centrifuged @12,000 rpm for 15 min. To remove the impurities, the washing (2-3

times) of precipitates with distilled water was accomplished by centrifuging @10,000 rpm for 10 min. Lastly, to study the effect of drying and annealing on morphology of nanostructures, the prepared nanomaterials were dried under two distinct conditions. The drying in vacuum oven at 70^{o} C for 2 h resulted in nanosheets while overnight drying of in simple oven at 70^{o} C yielded nanorods of antimony oxychloride.

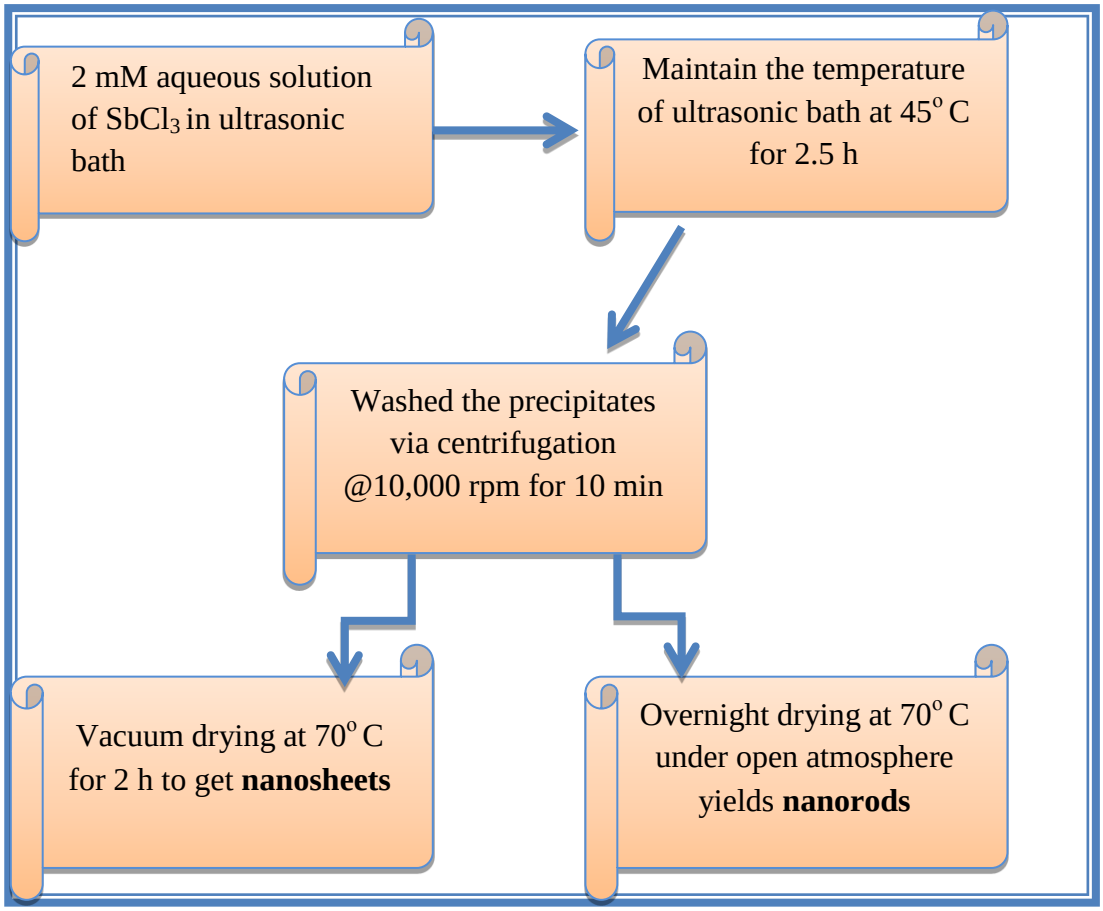

Figure 3.2: Graphical representation of synthesis of nano-antimony oxychloride

3.2.3 Synthesis of PNCs Thin films

The polymer based nanocomposite (PNC) of the prepared nanosheets and nanorods have been synthesized successfully. We have prepared the uniform thin films (PNC) with three different compositions (1, 3 and 5 w/w % of synthesized nanostructures) in PVA by facile solution casting method by following the synthetic strategy reported for MWCNT/PVA nanocomposites [70] without employing any catalyst. A 5 w/v% aqueous solution of PVA was prepared by continuous magnetic stirring at 40° C. When PVA was dissolved completely, antimony oxychloride nanosheets (1, 3 and 5 w/w %) relative to PVA was added in it. This solution was placed in ultrasonic bath for 2 h at 40° C to get the homogenous mixture. To remove air bubbles, the magnetically stirred solution was placed static for 1 h and subsequently poured solution was poured into washed petri dish and air dried in oven at 40° C for 2 days. Similar procedure was employed to prepare the thin films of PVA/antimony oxychloride nanorods of three different compositions (1, 3 and 5 w/w %). A thin film of neat PVA was also prepared as a reference.

Table 3.2 The synthetic route, reaction conditions and morphology obtained

Sample	**Parameters studied**		**Synthesis Method**	**Annealing conditions temperature (^{o} C)/time (h)**	**Morphology Obtained**
Bulk			Solubility difference method	Room temperature	Large Crystals
Microstructure	Concentration effect	1 mM	Precipitation method	60 / 0.5	Microstructures
		2 mM		60 / 0.5	Microstructures
		3 mM		60 / 0.5	Microstructures
	Ultrasonication effect	1 h	Precipitation method	60 / 1	Microstructures
Nanostructures	Effect of drying and annealing conditions	Vacuum drying at 70^{o} C for 2h	Precipitation method	45 / 2.5	Nanosheets
		Overnight drying at 70^{o} C in air	Precipitation method	45./ 2.5	Nanorods

$Sb_4O_5Cl_2$ nanosheets/PVA	Concentration effect	1 w/w%	Solution casting method	40 / 2.5	Thin film
		3 w/w%	Solution casting method	40 / 2.5	Thin film
		5 w/w%	Solution casting method	40 / 2.5	Thin film
$Sb_4O_5Cl_2$ nanorods/PVA		1 w/w%	Solution casting method	40 / 2.5	Thin film
		3 w/w%	Solution casting method	40 / 2.5	Thin film
		5 w/w%	Solution casting method	40 / 2.5	Thin film

3.3 Synthesis Chemistry

The bulk antimony oxychloride has been synthesized by simple solubility difference method. Antimony (III) trichloride is completely soluble in acetone while insoluble in water that is why $SbCl_3$ was added in acetone to make clear solution and forms a complex with acetone. When aprotic solvent added in the presence of base, charge transfer takes place and $Sb_4O_5Cl_2$ was obtained as a major product. The detailed reaction is given below,

$$SbCl_3 + (CH_3)_2CO \longrightarrow [(CH_3)_2ClC\ O^-]Sb^+Cl_2$$

$$[(CH_3)_2ClC\ O^-]Sb^+Cl_2 + H_2O \longrightarrow [(CH_3)_2OHC\ O^-]Sb^+Cl_2 + HCl$$

$$[(CH_3)_2OHC\ O^-]Sb^+Cl_2 + NaOH \longrightarrow Sb_4O_5Cl_2{+}(CH_3)_2CO + NaCl + H_2O$$

Overall reaction is

$$4SbCl_3 + (CH_3)_2CO + H_2O + 5NaOH \longrightarrow Sb_4O_5Cl_2 + (CH_3)_2CO + 5NaCl + H_2O + 5HCl$$

The above reaction details show that acetone and water act as solvent, while sodium hydroxide was employed as a structure directing agent.

The chemistry behind the synthesis of nanostructures of $Sb_4O_5Cl_2$ is simple hydrolysis reaction [71]. By the addition of $SbCl_3$ in a protic solvent like water, it becomes hydrolyzed to give antimony oxychloride.

$$4SbCl_3 + 5H_2O \longrightarrow Sb_4O_5Cl_2 + 10HCl$$

3.4 Characterization

X-ray powder diffraction data were collected from each compound in as-cast and annealed state employing a Model STOE Germany operating at 40 kV and 40 mA using monochromatic $Cuk_{\alpha 1}$ radiation in the range of ($10^o<2\theta<100^o$). The powder samples were coated with graphite using standard procedures and scanning electron microscopy (SEM) via Electron Probe Micro-Analyses (EPMA) has been performed on an MIRA3 TESCAN Zeiss Supra 55 VP equipped with an EDX system operated at 10 kV. The distance of electron beam from the sample is 6.35 mm.

The IR analysis carried out by PLATINIUM-ATR Model: ALPHA. Optical properties have measured by PerkinElmer UV/VIS/NIR spectrometer Lambda 950 having the spectral range of 190-3300 cm^{-1}. The powder samples was placed in sample holder to scan the reflectance. The pellets of 12 mm diameter with thickness of 2.3 mm were made by hydraulic press under pressure of 5 ton. Then these pellets were fixed one by one between electrodes. Wayne Kerr model 6500B LCR meter having frequency range of 100 Hz - 5 MHz was employed for these measurements. The dielectric properties were measured at room temperature.

Chapter 4

Results and Discussion

This chapter includes the detailed results of synthesis, characterization, optical and dielectric properties of the nano and bulk antimony oxyhalides materials.

4.1 XRPD & SEM Results

4.1.1 XRPD Results

XRPD has been employed to confirm the phase, crystal structure and the crystallite size of bulk and nanostructures. The detailed analysis confirmed the structure type $Sb_4O_5Cl_2$ with monoclinic symmetry in space group $P2_1/C$ no. 14 for both; bulk and the nanostructures. Table 4.1 depicts the lattice parameters, density and cell volume obtained with generalized harmonic description during Rietveld refinement. The number in parentheses gives the estimated standard deviation for the least significant figure of the parameter. The refined structural parameters agreed quite well with the corresponding single-crystal results [43]. Additional refinement of background has carried out via linear interpolation between set background points with definable heights, upon selected and saved points in a separate file type.bgr. This confirmed the purity of prepared nano-morphologies and bulk antimony oxyhalides.

Table 4.1 Lattice parameters of prepared sample

Sample Type	Lattice parameters (Å)			β (°)	Density (g/cm^3)	Cell Volume (Å^3)	Ref.
	a	b	c				
Nanosheets	6.225(1)	5.103(1)	13.512(3)	97.24(1)	5.30	426.1(1)	[This work]
Nanorods	6.2360(6)	5.1080(7)	13.530(7)	97.221(6)	6.84	427.57(9)	[This work]
SC*	6.2380(4)	5.1112(3)	13.538(2)	97.217(8)	4.95	428.22	[52]

Bulk	6.2395(2)	5.1213(2)	13.5304(5)	97.2439(7)		428.90(4)	[This work]
SC	6.2410(2)	5.1139(2)	13.5357(5)	97.2380(7)	5.25	428.56(3)	[This work]

*SC-single Crystal data.

The goodness of fit index (χ^2) values are 1.24 and 1.04 for nanosheets and nanorods, respectively. Variation in lattice parameters and unit cell volume is obvious in the data presented in table 4.1 which is mainly due to the different oxygen contents in bulk, nanorods and nanosheets. Figures 4.1 & 4.2 show the agreement between the calculated and measured XRD patterns for the nanorods and nanosheets, following Rietveld refinement method with the generalized harmonic description for preferred orientation and symmetry correction.

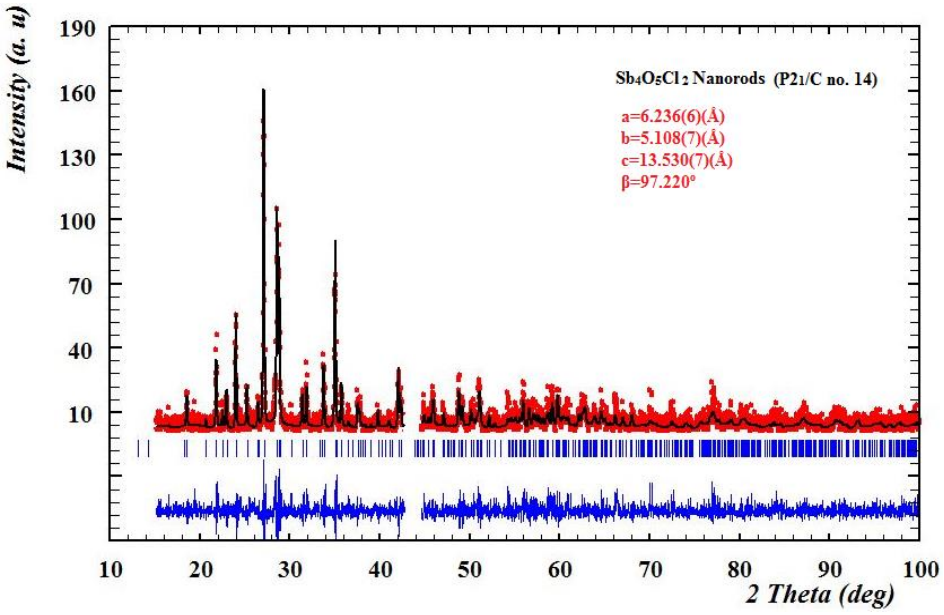

Figure 4.1: Refined XRPD pattern of Nanorods

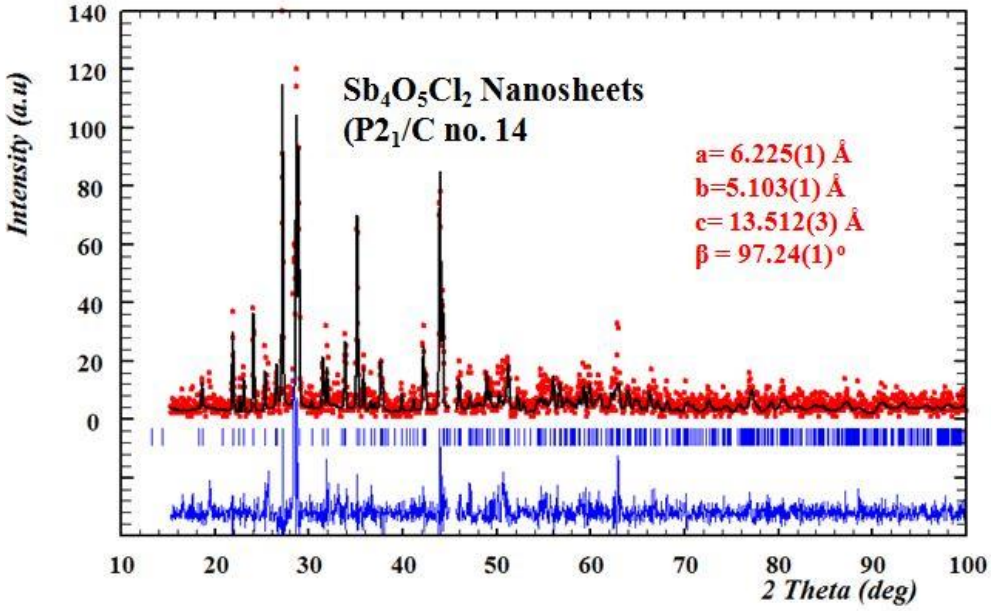

Figure 4.2: Refined XRPD pattern of Nanosheets

Further figure 4.3 obtained from WinPloter, shows the comparison among the nanorods and nanosheets $Sb_4O_5Cl_2$. The patterns show that all the peaks are identical but the intensity of peaks is higher in the case of nanosheets which are due to the preferred orientation of particles along (001).

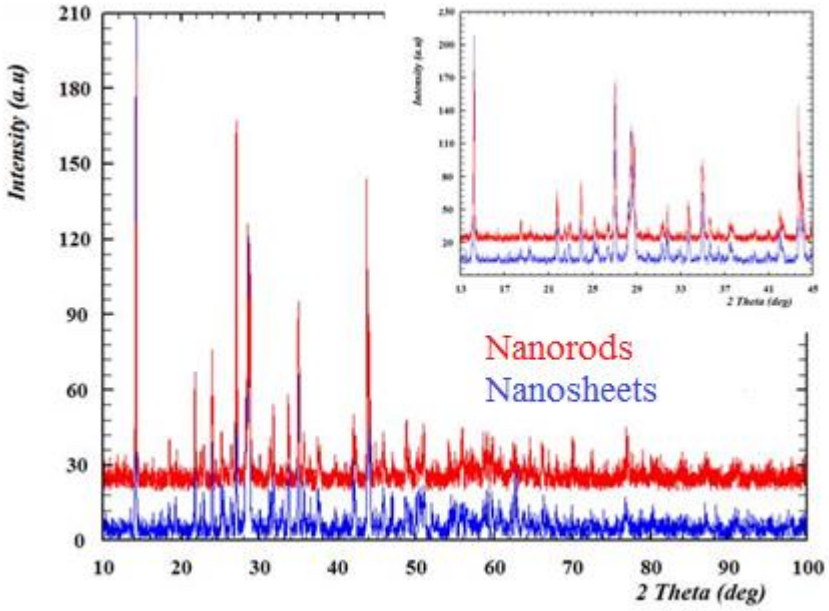

Figure 4.3: Comparison among XRPD of nanostructures of $Sb_4O_5Cl_2$

Debye–Scherrer Formula is most commonly used method to calculate the crystallite size provided here [72],

$$\mathbf{D} = \frac{K\lambda}{\beta \mathbf{Cos}\theta}$$

Where

K = 0.94

λ = 0.154 nm

β = FWHM

It is a quick method to determine the crystallite size but it never takes into account the peak broadening contribution due to micro-strain and the instrument. In Scherrer equation, β parameter is full-width half maxima (FWHM) of observed peaks. Its value

not only depends upon the material itself but also affected by instrument and micro-strains in structure. Cullity et al. in 1978 has formulated an expression to calculate the instrumental effect correction that is [73],

$$\beta = \sqrt{\beta_{exp}^2 - \beta_{standard}^2}$$

The micro-strains contribution towards the line broadening of diffraction peaks (β_ε) has been determined by A. W Burton in 2009. The β_ε is measured by using formula,

$$\beta\varepsilon = 4\varepsilon tan\theta$$

To calculate the corrected value of β, the following equation is used

$$\beta = \beta\varepsilon \pm \beta_D$$

Another convenient method to nullify the effect of micro-strains is Williamson-Hall (WH) plot [74] which is a plot between $sin\theta$ and $\beta cos\theta/\lambda$. The value of intercept and slope gives the particle size and micro-strain respectively. The positive slope shows the lattice expansion, while negative slope indicates the lattice compression and horizontal slope specifies the presence of perfect crystal free of micro-strain [75]. The WH-plots for nanosheets, nanorods and bulk have provided below

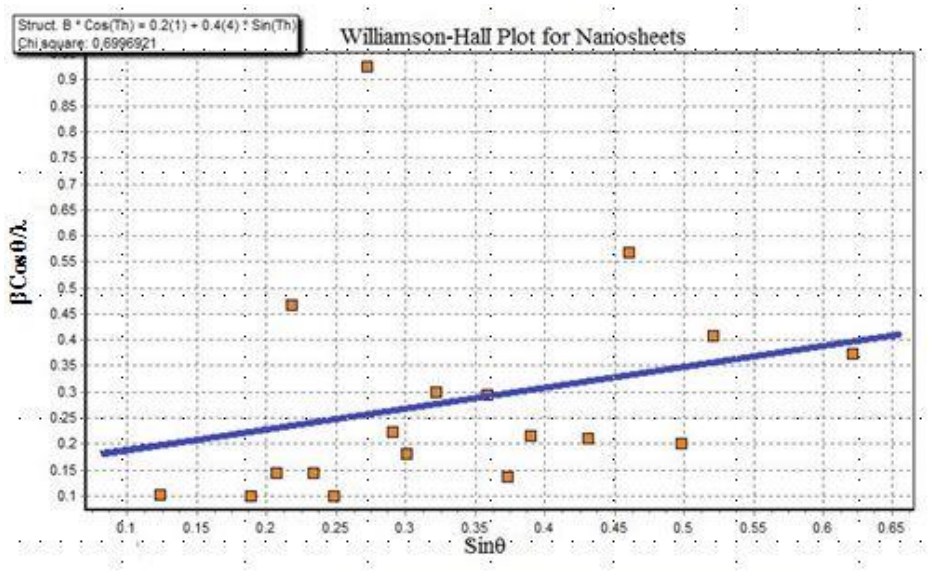

Figure 4.4: WH Plot for nanosheets

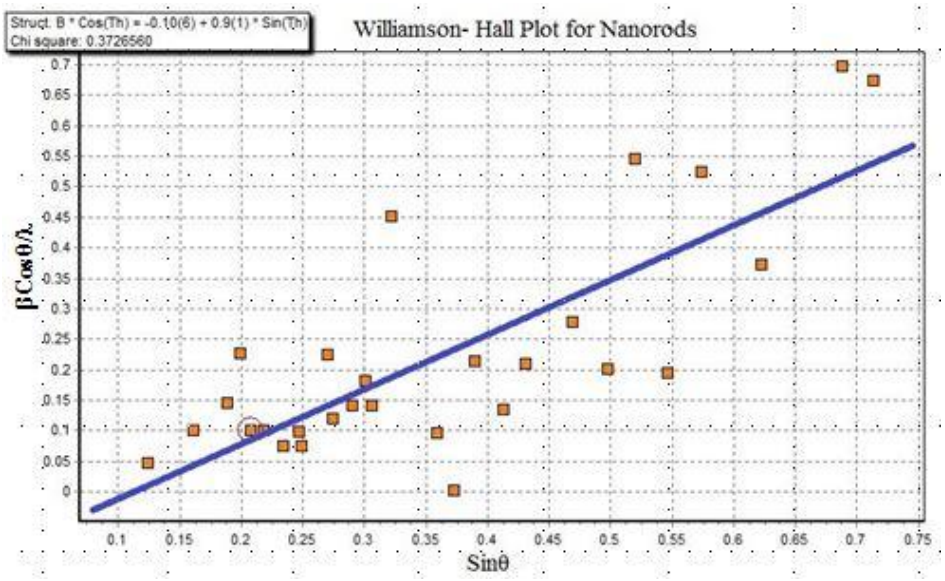

Figure 4.5: WH Plot for nanorods

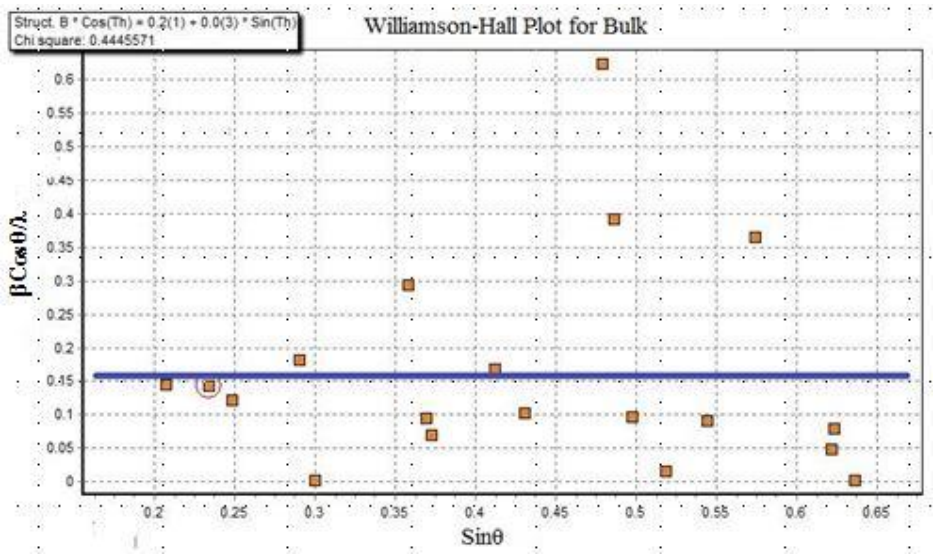

Figure 4.6: WH plot for Bulk

The table 4.2 shows the comparison among crystallite size calculated form Scherrer equation and WH- plot.

Table 4.2 Crystallite size calculated form Debye-Scherrer equation and WH plot

(hkl)	**Crystallite size (nm)[#]**			**Crystallite size (nm)/Strain (%)[##]**		
	NS[*]	NR[*]	Bulk	NS[*]	NR[*]	Bulk
(-211)	53.2	107.2	71			
(-124)	55.3	55.3	77	57.2/	90.7/	104.2/
(312)	56.4	56.4	137.6	0.2(2)	0.39(6)	0.0(1)
(400)	58.7	58.7	143			

[*]NS and NR stand for nanorods and nanosheets, respectively. [#] calculated from Debye–Scherrer formula, [##] calculated from WH-Plot.

4.1.2 SEM Results

The qualitative analysis and morphology of the samples were determined by SEM. The SEM micrograph of the microstructures, nanosheets and nanorods of antimony

oxychloride are shown in figure 4.7, 4.8 and 4.9. The morphology and compositions of prepared microstructures by varying the precursor concentration and ultrasonication time (1 h) have been provided in figure 4.6. These images confirm that the prepared particles have composition $Sb_{35.36}$ $O_{50.33}$ $Cl_{14.3}$ at % and size in micro range. Moreover, these analysis have also delivered information about the microstructures of antimony oxychloride prepared with (*2 mM)* are more fine as compare to other two concentrations. Further ultrasonication helps us to reduce the size and avoid agglomeration of the particles. In figure 4.8, where a and b images represented the overall morphology and composition while figure 4.8c shows that one dimension of nanosheets which lies in a range of 50-150 nm with the $Sb_{33.28}$ $O_{52.28}$ $Cl_{12.5}$ at %. The extra peaks in EDX spectra can be attributed to sample holder and graphite coating material. Similarly, fig 4.9a and b parts show the overall morphology and composition of antimony oxychloride nanorods while 1D nanorods confirmed by figure 4.9c with the composition $Sb_{33.73}$ $O_{50.73}$ $Cl_{15.54}$ at %. The synthesized nanorods have *l* ~2 µm and dia. = 50-90 nm. The EDS spectra of antimony oxychloride exhibited the ratio of Sb:O:Cl is 2:3:1 for nanosheets as well as nanorods.

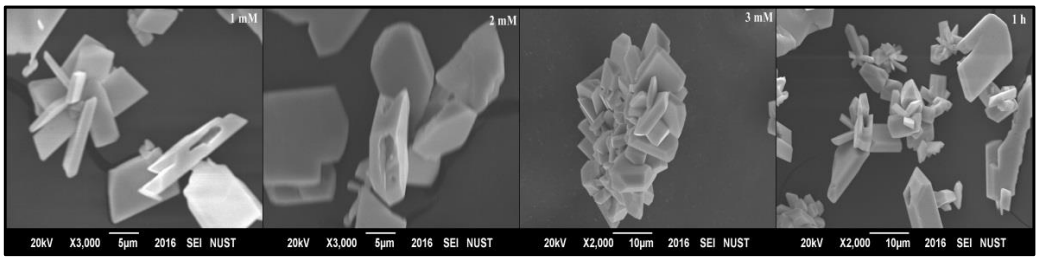

Figure 4.7: SEM micrographs of antimony oxychloride microstructures prepared with different concentrations and ultrasonication time

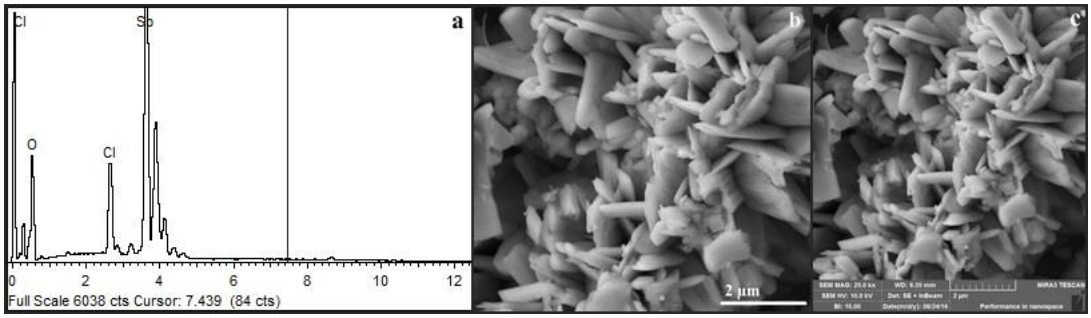

Figure 4.8: SEM micrographs of antimony oxychloride nanosheets with EDX spectrum

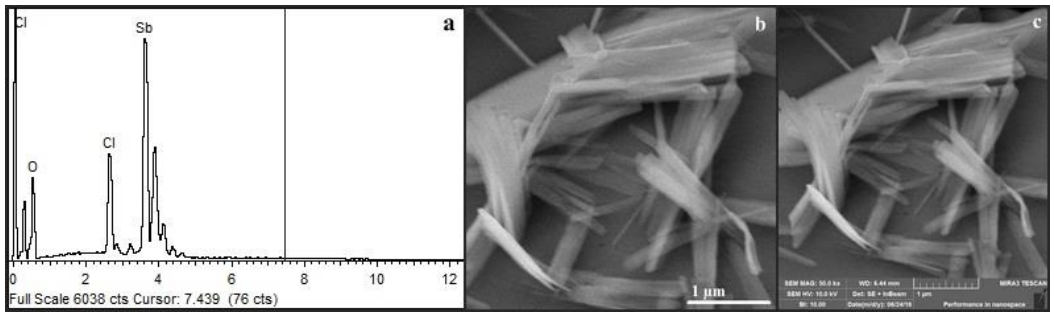

Figure 4.9: SEM micrographs of antimony oxychloride nanorods with EDX spectrum

The table below shows the dimensions obtained from SEM data.

Table 4.3Dimeniонsions and %age composition from SEM

Sample Type	SEM composition (at%<± 2 esd)			Dimensions (SEM)
	Sb	O	Cl	
Microstructures	35.36	50.33	14.3	Thickness ~ 2-3 µm *l*~ 5-10 µm
Nanorods	33.73	53.73	15.54	dia = 50-90 nm *l* ~2 µm
Nanosheets	35.28	52.28	12.5	Thickness = 50-150 nm *l* ~2 µm
Bulk	35.61	46.62	18.02	<500 µm

4.1.2.1 Annealing Conditions & Morphology of Nanostructures

Various studies have proved that the morphology of nanostructures depend upon the reaction time & temperature, drying conditions and annealing temperature & time [76-78]. The effect of drying time has been studied over the morphology of different nanostructures. The results of SEM analysis revealed that with the increase in drying time (from 2 to 17 h) nanostructures change morphology from NS to NR because atoms have more time to get aligned. Therefore atoms of Sb, O, and Cl arranged themselves along crystallographic preferred orientation and gave branches. This kind of preferred orientations of crystallites have been observed in XRPD patterns of NR where the greater intensity of peaks along (110), (111), (013) and (300) plans have been observed. By comparing the XRPD pattern and SEM analysis, it has been verified that as drying time increases the length of nanosheets increases consequently decreasing the diameters which leads to morphology changes from NS to NR.

4.1.3 IR Analysis

FTIR analysis has been carried out to confirm the synthesis of $Sb_4O_5Cl_2$ nanostructures/PVA composites. The IR spectra of individual $Sb_4O_5Cl_2$ nanosheets, nanorods, PVA and nanocomposite have been provided below in figures 4.10, 4.11 and 4.12. The IR spectra of $Sb_4O_5Cl_2$ nanostructures (nanosheets and nanorods) are comparable except variation in peak intensities. The IR spectrum of above mentioned compounds show that separate bands for $Sb_4O_5Cl_2$ and PVA are present in case of PNCs. The presence of individual bands verifies that there is no chemical reaction taking place during the synthesis of composites. A simple physical interaction has built up between the nanostructures of $Sb_4O_5Cl_2$ and PVA. Figure 4.12 also shows that as the weight % of nanomaterial in PNCs increases the bands intensity of PVA peaks decreases successively.

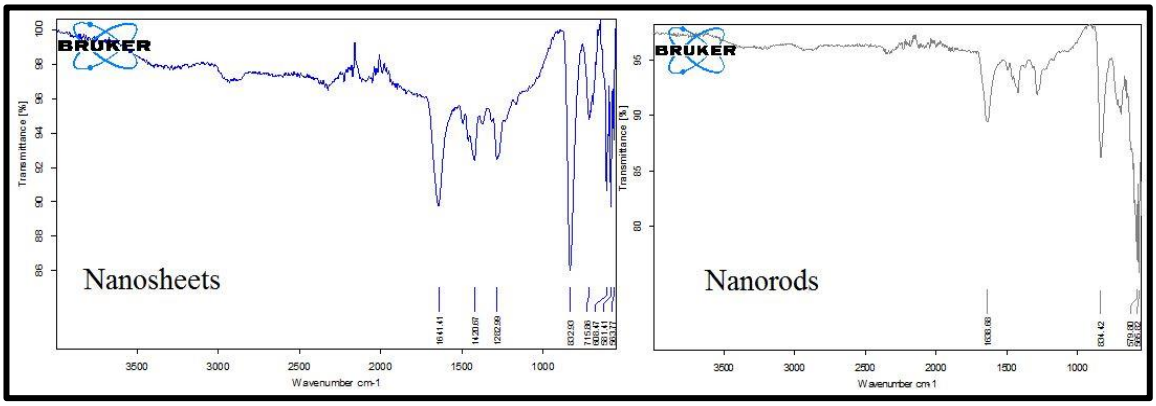

Figure 4.10: IR spectra of $Sb_4O_5Cl_2$ nanosheets and nanorods

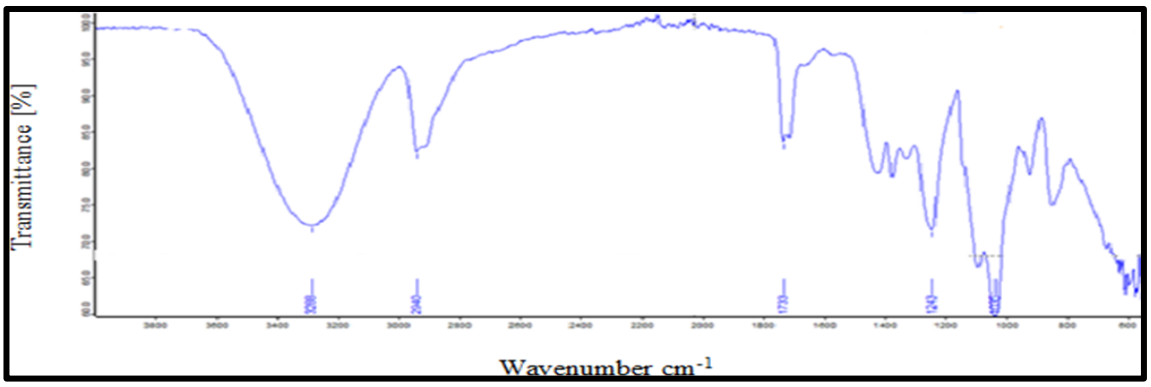

Figure 4.11: IR spectrum of PVA thin film

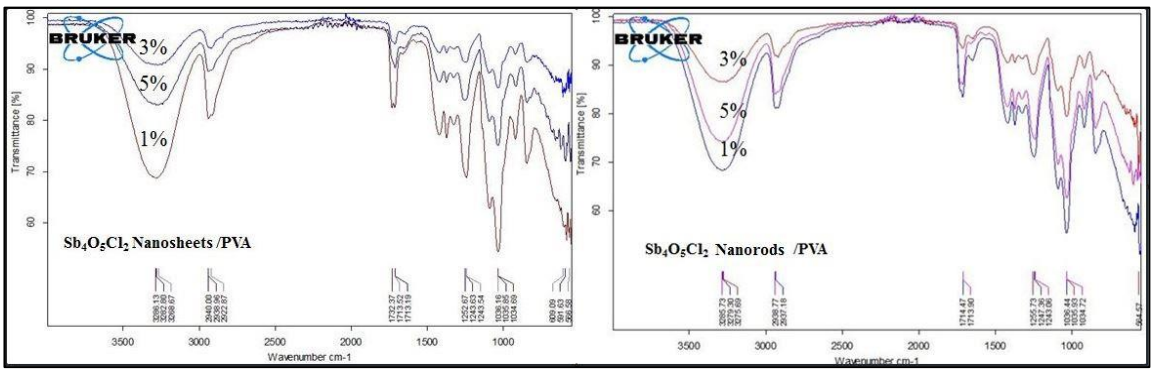

Figure 4.12: IR spectra of $Sb_4O_5Cl_2$ Nanosheets/PVA and $Sb_4O_5Cl_2$ Nanorods/PVA films with different composition

4.2 Properties

4.2.1 Optical Properties

Simple UV-Vis absorption spectroscopy has not proved much useful for the optical properties of antimony oxychloride nanomaterial. No doubt the particle size was reduced up to nanometer but it was difficult to get an ideal suspension of antimony oxychloride in any solvent. Whereas, DRS UV (Diffused Reflectance Spectroscopy Ultra violet) has proved a better technique for calculation of the optical properties and to ascertain the band gap. The electronic band gap of resulting nanosheets and nanorods have measured via DRS UV and compared with that of the bulk. In reflectance spectra provided in figure 4.13a, it is obvious that maximum reflectance occurred at about 405 nm. Further this study reveals that nanostructures of antimony oxychloride have better reflectance ability as compared to its bulk counterpart. The DRS UV study also allows the calculation of band gap through Tauc's plot (a plot of energy (eV) Vs $(h\nu\alpha)^n$) [79]. In DRS UV, the absorption factor is replaced by reflectance factor $F(R)$ and it can be calculated by using Kubelk-Munk expression given below [80],

$$F(R) = \frac{(1-R)^2}{2R} = \frac{K}{S}$$

Where

R-Absolute Reflectance

K-Molar absorption co-efficient

S-Scattering co-efficient

A plot of Energy (eV) Vs $h\nu F(R)^2$ has been plotted to approximate the value of E_g, figure 4.13b shows a graph having estimated values of band gap for nanorods, nanosheets

and bulk form of antimony oxychloride that is 3.34, 3.31 and 3.25 eV, respectively. These results disclosed that as we move from bulk to nano-antimony oxychloride, the band gap increases from 3.25 to 3.34 eV.

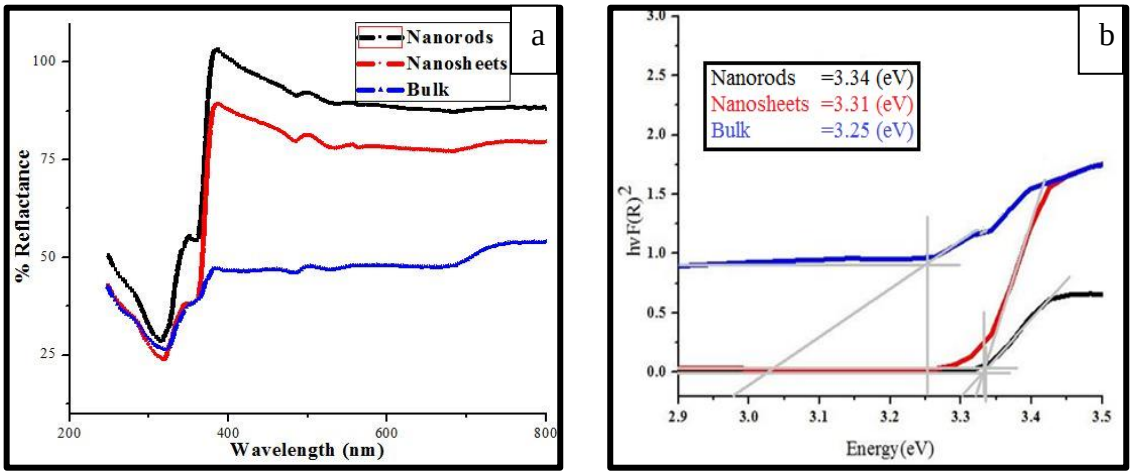

Figure 4.13: (a) A plot of wavelength and %reflection of different nanostructures of antimony oxychloride. (b) Shows the band gap values of nanosheets, nanorods and bulk antimony oxychloride

In the case of bulk $Sb_4O_5Cl_2$, a greater number of adjacent energy levels overlap give a continuous energy bands. While in the case of nanostructures of $Sb_4O_5Cl_2$, a finite number of energy levels lead to the decrease in a number of overlapped orbitals, resulting in discrete energy levels. So nanostructures have discrete (quantized) energy levels instead of continuous ones. This causes the enhanced band gap due to the confinement of electronic wave function to the physical dimensions of the particles [81]. Therefore we have observed the decrease in the band gap value as particle size increases or vice versa. The $Sb_4O_5Cl_2$ nanorods have the smallest particle size and have largest band gap value *i.e.* is 3.34 eV while bulk has the highest particle size and the lowest value of band gap *i.e.* is 3.25 eV.

4.2.2 Dielectric Properties

The word dielectric is the combination of two words that means "No effect of direct electric field or applied electric field". Dielectric materials are those which do not show any response toward an incoming electric field. Therefore insulators and semiconductors fall in the category of dielectric materials. Dielectric properties are comprised of four main components that are dielectric constant, dielectric loss, tangent loss and AC conductivity as these are the important parameters to explore device application of materials. Dielectric constant (ε) provides information about the ability of material to become polarize (polarizability of material) or capacity of material to store applied electric energy. Mainly, it is the ratio of the permittivity of material to that of the vacuum. The value of dielectric has been calculated by using expression following

$$\varepsilon = \frac{C \times d}{\varepsilon_o \times A}$$

Where C is capacitance, d is the sample thickness, ε_o is permittivity of free space having value $8.85\times10^{-}12$ Fm^{-1} and A is the surface area of the sample [82]. Dielectric loss (ε') or dissipation factor is an imaginary part to determine the loss of electromagnetic energy or the electromagnetic energy that is dissipated to align the particles along applied electric field. The real part to calculate the energy loss is called tangent loss ($tan\delta$) while dissipation factor quantitatively parameterized by using the term known as tangent loss factor. The equations to measure these two factors are given below [83, 84].

$$\varepsilon'' = \varepsilon \times D.factor$$

$$tan\delta = \frac{\varepsilon''}{\varepsilon}$$

Lastly, AC conductivity (σ_{ac}) is the capacity or ability of material to allow the passage of alternating current which can be calculated σ_{ac} by the below given formula,

$$\sigma_{ac} = 2\pi f \varepsilon_o \varepsilon' tan\delta$$

Out of the four types of polarization, *i.e*. electronic, ionic/atomic, dipolar or orientational and interfacial polarization, we usually come in contact with a dipolar or orientational polarization which takes place at the frequency about 1 k-1 MHz. The plot of ln (F) and ε (given in fig 4.10a) shows a higher value of ε for nanosheets (~87) as compare to nanorods (~40) and bulk (~35.5). Nanosheets of antimony oxychloride show an ideal response towards applied electric field and the value of dielectric constant goes on decreasing with increasing frequency because at the higher frequency the molecules have no time to orient themselves according to applied field. Therefore, they allow the passage of electrons and become conducting. While in the case of nanorods and bulk form of antimony oxychloride, there is no significant effect of frequency so the value of dielectric constant almost remains same for the whole frequency range. A similar trend for dielectric loss and tangent loss has observed for nanosheets, nanorods and bulk antimony oxychloride as provided in figure 4.14b and 4.14c. The measured value of dielectric loss for nanosheets, nanorods and bulk are 40, 1.4 and 0.5, respectively. The tan loss is 1.2 in case of nanosheets and approximately near to zero for nanorods and bulk antimony oxychloride. Another important component to determine dielectric behviour is AC conductivity. A graph between ln(F) and AC conductivity helps to measure the AC conductivity of material shown in figure 4.6d which depicts higher value of AC conductivity at lower frequency (5 kHz) in case of nanosheets, because the particles can easily align themselves to applied field and permits the flow of electrons. But at a higher frequency (7 kHz), the molecules do not have enough time to orient themselves with the applied field. At high frequency, AC conductivity decreases due to arbitrary motion of molecules in all directions and cause resistance along passage of current. Nanorods and bulk do not have such a prominent response towards AC conductivity. At highest frequencies (12 kHz), a phenomenon of hopping is observed in all three cases with the most prominent one in bulk case. When the frequency of electron transfers, from one

atom to another atom in the same molecule, becomes equal to the applied frequency, resonance takes place. This resonance causes the enhancement in amplitude that is observed in form of hop in the graph. This is may be due to some defect in structure etc.

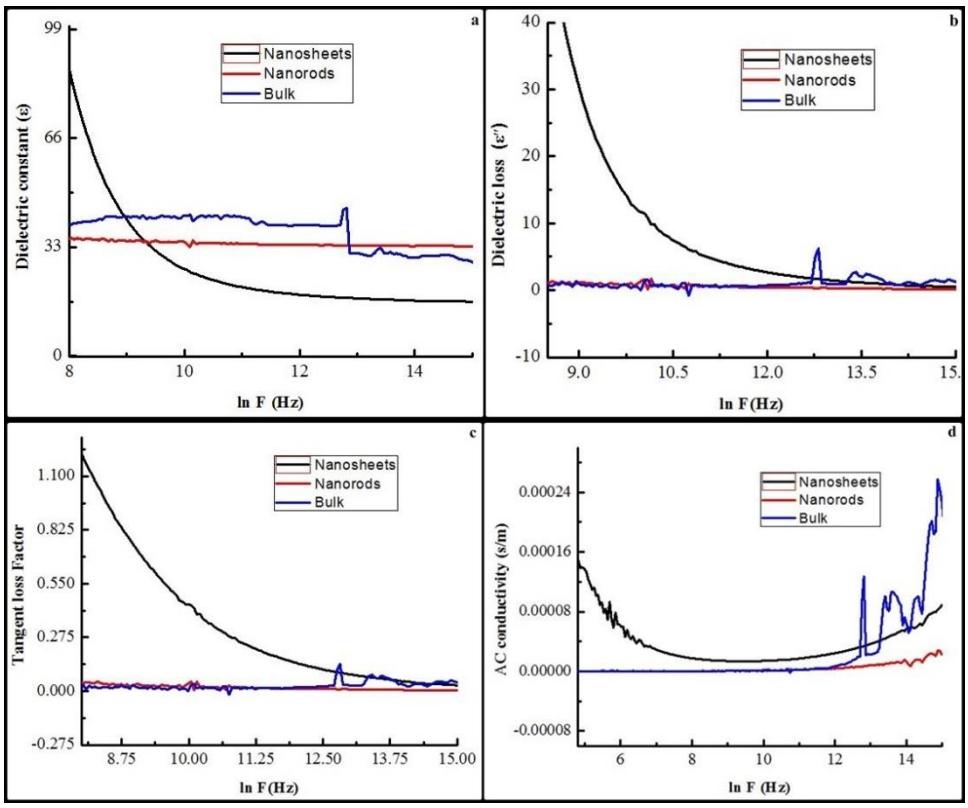

Figure 4.14: (a) Plot of ln (F) and dielectric constant. (b) Plot between ln (F) and dielectric loss. (c) Graph of ln (F) and tan loss factor and (d) plot of ln (F) and AC conductivity

4.3 Conclusions and Future prospects

Different nanoforms, microstructures and the bulk single phase materials of $Sb_4O_5Cl_2$ have been prepared by using single precursor via simple wet chemical strategy. The composition, morphology, geometry, crystal structure and crystallite size of materials have been investigated by employing XRPD, EDX spectra and the SEM analysis. Further, optical and dielectric properties of nanorods and nanosheets along with comparison with the bulk counterpart has been studied. Optical properties clearly show that nanorods of $Sb_4O_5Cl_2$ have highest band gap, *i.e.* 3.34 eV as compared to those of nanosheets and the bulk (3.31 and 3.25 eV, respectively). These properties depicts that $Sb_4O_5Cl_2$ is a semiconductor whose band gap increases as we move from bulk to nanoregime. In the case of nanosheets, the highest value of dielectric constant has been observed, *i.e.* 87 as compared to that of nanorods and the bulk, 40 and 35.5, respectively. These nanosheets have also shown that the highest value of dielectric and tangent loss along with the increase in frequency due to the least crystallite size of this material. Nanosheets have depicted higher AC conductivity at the low frequency while nanorods and bulk material had no change throughout the frequency range. The hopping phenomenon has been observed in all three cases with the most prominent one in bulk case at higher frequencies. The PNCs is synthesized by using PVA as matrix for various compositions (1, 3 and 5 w/w%) of $Sb_4O_5Cl_2$ nanorods and -sheets. IR analysis has confirmed the synthesis of composites.

These properties; semiconducting nature, smaller crystallite and particle size make these materials the potential candidates in energy storage devices and the better flame retardants. The bulk form of this material is reported as a flame retardant material, so in future this material can be used for synthesis of nanocomposite with different polymers which may prove valuable materials for wire coating and textile industry.

References

[1] Gribbin, John and M. Gribbin. "Richard Feynman: A Life in Science. Dutton," **17**, (1997).

[2] J. S. Tsuji, A. D. Maynard, P. C. Howard, J. T. James, C. W. Lam D. B. Warheit and A. B. Santamaria, "Research Strategies for Safety Evaluation of Nanomaterials: Risk Assessment of Nanoparticles," *Toxicological Sciences,* **89**, 42-50 (2006).

[3] K. Y. Rajpure, C .H. Bhosale, "Effect of Composition on the Structural, Optical and Electrical Properties of Sprayed Sb_2S_3 Thin Films Prepared from Non-Aqueous Medium," *Journal of Physics and Chemistry of Solids,* **61,** 561–568 (2000).

[4] D. B. Salunkhe, S. S. Gargote, D. P. Dubal, W. B. Kim, B. R. Sankapal, Sb_2S_3 Nanoparticles Through Solution Chemistry on Mesoporous Tio_2 for Solar Cell Application," *Chemical Physics Letters*, **554,** 150–154 (2012)

[5] Z. Zhang, C. Zhou, Y. Liu, J. Li, Y. Lai and M. Jia, "$CuSbS_2$ Nanobricks as Electrode Materials for Lithium Ion Batteries," *Int. J. Electrochem. Sci*., **8**, 10059–10067 (2013).

[6] R. Roy, R. A Roy and D. M Roy, "Alternative Perspectives on "Quasi-Crystallinity": Non-Uniformity and Nanocomposites," *Materials Letters*, **4**, 323-328 (1986).

[7] P. H. C. Camargo, K. G. Satyanarayana, F. Wypych, "Nanocomposites: Synthesis, Structure, Properties and New Application Opportunities, *Materials Research*, **12**, 1-39, (2009).

[8] A. B. Morgan, Flame Retarded Polymer Layered Silicate Nanocomposites: A Review of Commercial and Open Literature Systems, *Polymers for Advanced Technologies*, **17**, 206–217 (2006).

[9] K. C. See, J. P. Feser, C. E. Chen, A. Majumdar, J. J. Urban and R.A. Segalman, "Water Processable Polymer Nanocrystal Hybrids for Thermoelectrics", *Nano Lett.,* **10**, 4664–4667 (2010).

[10] A. Arora and G.W. Padua, "Review: Nanocomposites in Food Packaging," *Journal of Food Science*, **Nr. 1**, 43-48 (2010).

[11] Y. T. Wang, S. F. Liao, K. Shang, M. J. Chen, J. Q. Huang, Y. Z. Wang and D. A. Schiraldi, "Efficient Approach to Improving the Flame Retardancy of Poly(vinylalcohol)/Clay Aerogels: Incorporating Piperazine-Modified Ammonium Polyphosphate," *ACS Appl. Mater. Interfaces,* **7**, 1780−1786 (2015).

[12] B. Yuan, C. Bao, Y. Guo, L. Song, K. M. Liew and Y. Hu, "Preparation and Characterization of Flame-Retardant Aluminum

References

Hypophosphite/Poly(Vinyl Alcohol) Composite," *Ind. Eng. Chem. Res.*, **51**, 14065−14075 (2012).

[13] H. Qin, S. Zhang, C. Zhao, G. Hu, M. Yang, "Flame Retardant Mechanism of Polymer/Clay Nanocomposites Based on Polypropylene," *Polymer*, **46** 8386–8395 (2005).

[14] T. M. Tritt, "Thermoelectric Phenomena, Materials and Applications," *Annu. Rev. Mater. Res*., **41**, 433–448 (2011).

[15] K. Fujihara, A. Kumar, R. Jose, S. Ramakrishna, S. Uchida, "Spray deposition of electro spun TiO_2 nanorods for dye-sensitized solar cell," *Nanotechnology*, **18,** 365709 (2007).

[16] S. Suehiro, K. Horita, M. Yuasa, T. Tanaka, K. Fujita, Y. Ishiwata, K. Shimanoe and T. Kida, "Synthesis of Copper−Antimony-Sulfide Nanocrystals for Solution-Processed Solar Cells," *Inorg. Chem*. **54,** 7840−7845 (2015).

[17] M. S. Rahaman, C. D. Vecitis and M. Elimelech, "Electrochemical Carbon-Nanotube Filter Performance toward Virus Removal and Inactivation in the Presence of Natural Organic Matter," *Environmental Science & Technology*, **46**, 1556-1564 (2012).

[18] M. Auffan, J. Rose, O. Proux, D. Borschneck, A. Masion, P. Chaurand, J. L. Hazemann, C. Chaneac, J. P. Jolivet, M. R. Wiesner, A. Van Geen, J. Y. and Bottero, "Enhanced Adsorption of Arsenic onto Maghemites Nanoparticles: As(III) as a Probe of the Surface Structure and Heterogeneity," *Langmuir*, **24**, 3215-3222 (2008).

[19] A. Becheri, M, Durr, P. L. Nostro, P. Baglioni, "Synthesis and Characterization of Zinc Oxide Nanoparticles Application to Textiles as UV-Absorbers," *J. Nanopart. Res.*, **10,** 679–689 (2008).

[20] J. K. Patra and S. Gouda, "Application of Nanotechnology in Textile Engineering: An Overview," *Journal of Engineering and Technology Research*, **5**, 104-111 (2013).

[21] A. P. Nikalje, "Nanotechnology and its Applications in Medicine," *Med. Chem. 2015*, **5**, (2015).

[22] L. Zhang, F. X. Gu, J. M. Chan, A. Z. Wang, R. S. Langer and O. C. Farokhzad, "Nanoparticles in Medicine: Therapeutic Applications and Developments," *Clinical Pharmacology and Therapeutics*, **83**, 761-769 (2008).

[23] J. Seo, J. Jang, S. Park, C. Kim, B. Park and J. Cheon, "Two-Dimensional SnS_2 Nanoplates with Extraordinary High Discharge Capacity for Lithium Ion Batteries,"*Adv. Mater*., **20**, 4269−4273 (2008).

[24] J. V. Embden, K. Latham, N. W. Duffy and Y. Tachibana, "Near-Infrared Absorbing $Cu_{12}Sb_4S_{13}$ and Cu_3SbS_4 Nanocrystals: Synthesis, Characterization, and Photoelectrochemistry," *J. Am. Chem. Soc*., **135**,

11562−11571 (2013).

[25] F. Haguenau, P. W. Hawkes, J. L. Hutchison, B. Satiat-Jeunemaître, G. T. Simon and D. B. Williams, "Key Events in the History of Electron Microscopy," *Microscopy and Microanalysis*, **9**, 96-138 (2003).

[26] W. Zhou, Z. L. Wang (Eds.), "Scanning Microscopy for Nanotechnology: Technique and Applications," *Springer Science and Business Media, New York* 1–40 (2007).

[27] C. T. K. H. Stadtländer, "Scanning Electron Microscopy and Transmission Electron Microscopy of Mollicutes: Challenges and Opportunities," *Modern Research and Educational Topics in Microscopy*, Formatex, Badajoz, 121-131 (2007).

[28] R. Das, M. E. Ali and S. B. A. Hamid, "Current Applications of X-Ray Powder," *Rev. Adv, Mater. Sci*, **38**, 95-109 (2014).

[29] W. Kraus, G. Nolze, "POWDER CELL- A Program for the Representation and Manipulation of Crystal Structures and Calculation of the Resulting X-Ray Powder Patterns," *J. Appl. Crystallogr*., **29**, 301-303 (1996).

[30] T. Roisnel and J. Rodriguez-Carvajal, "WinPLOTR: A Windows Tool for Powder Diffraction Pattern Analysis," *Materials Science Forum*, 378-381 118-123 (2001).

[31] H. M. Rietveld, "A Profile Refinement Method for Nuclear and Magnetic Structures," *Journal of applied Crystallography*, **2**, 65-71 (1969).

[32] B. Stuart, "Infrared Spectroscopy," *Kirk Othmer Encyclopedia of Chemical Technology*, (2005).

[33] A. E. Morales, E. S. Mora and U. Pal, "Use of Diffuse Reflectance Spectroscopy for Optical Characterization of Un-Supported Nanostructures," *Revista Mexicana Defisicas*, **53,** 18–22 (2006).

[34] R. K. Rajput, *Elect & Electronic Measurement & Instrument*. S. Chand Limited, (2009).

[35] U. A. Bakshi, A. V. Bakshi, "Electronic Measurement Systems," *Technical Publications*, (2009).

[36] Y. Liu, X. Yuan, H. Wang, X. Chen, S. Gu , Q. Jiang, Z. Wu, L. Jiang, Y. Wu and G. Zeng., "Novel Visible Light-Induced G-C_3N_4–Sb_2S_3/$Sb_4O_5Cl_2$ Composite Photocatalysts for Efficient Degradation of Methyl Orange," *Catal. Commun.* **70**, 17–20 (2015).

[37] N. Chand and S. Verma, *J Fire Sci*, **9,** 251–258 (1991).

[38] M. Walter, S. Doswald and M. V. Kovalenko, "Inexpensive Colloidal Snsb Nanoalloys as Efficient Anode Materials for Lithium and Sodium-Ion Batteries," *J. Mater. Chem. A*, **4**, 7053-7059 (2016)

[39] M. J. Buerger and S. B. Hendricks, *Z. Kristallographics*, **98**, 1-30 (1938).

[40] C. Svensson, "The Crystal Structure of Orthorhombic Antimony Trioxide," Sb_2O_3, *Acta. Cryst.* **B30**, 458- 461 (1974).

References

[41] J. P. Allen, J. J. Carey, A. Walsh, D.O. Scanlon and G.W. Watson, "Electronic Structures of Antimony Oxides," *J. Phys. Chem. C,* **117,** 14759−14769 (2013).

[42] S. Ge, Q. Wang, J. Li, Q. Shao, X. Wang, "Controllable Synthesis and Formation Mechanism of Bow-Tie-Like Sb_2O_3 Nanostructures via A Surfactant Free Solvothermal Route," *Journal of Alloys and Compounds***, 494,** 169–174 (2010).

[43] Z. Deng, F. Tang, D. Chen, X. Meng, L. Cao and B. Zou, "A Simple Solution Route to Single Crystalline Sb_2O_3 Nanowires with Rectangular Cross Sections," *J. Phys. Chem. B***, 110**, 18225-18230 (2006).

[44] L. Liu, Z. Hu, Y. Cui, B. Li, X. Zhou, A Facile Route to the Fabrication of Morphology Controlled Sb_2O_3 Nanostructures, *Solid State Sciences,* **12,** 882–886 (2010).

[45] S. Sun , J. Peng , R. Jin , S. Song , P. Zhu , Y. Xing, "Template-Free Solvothermal Synthesis and Enhanced Thermoelectric Performance of Sb_2Te_3 Nanosheets," *Journal of Alloys and Compounds,* **558**, 6-10 (2013).

[46] T. Cebriano, B. Méndez, J. Piqueras, "Micro and Nanostructures of Sb_2O_3 Grown by Evaporation Deposition: Self-Assembly Phenomena, Fractal and Dendritic Growth," *Materials Chemistry and Physics*, **135**, 1096-1103 (2012).

[47] Z. Deng, D. Chen, F. Tang, X. Meng, J. Ren and L. Zhang, Orientated Attachment Assisted Self-Assembly of Sb_2O_3 Nanorods and Nanowires: End-to-End Versus Side-by-Side, *J. Phys. Chem. C*, **111**, 5325-5330 (2007).

[48] L. Song, S. Zhang and Q. Wei, "Perfect, Sectorial, Branched Sb_2O_3 Microstructures Consisting of Prolate Microtubes: Controllable Seeded Growth Synthesis and Optical Properties," *Cryst. Growth Des*. **12**, 764−770 (2012).

[49] F. Li, W. Jianhuai, L. Jiongtian, W. Bingguo and S. Shuojiang, "Preparation and Fire Retardancy of Antimony Oxide Nanoparticles/Mica Composition," *Journal of Composite Materials*, **41**, 1487-1497 (2007).

[50] A. Astriim and S. Andersson, "The Crystal Structure of L-SbOF," *Journal of Solid State Chemistry*, **6**, 191-194 (1973).

[51] A. Astrom, "The Structure of M-SbOF," *Acta Chemica Scandinavica*, **26**, 3849-3854 (1972).

[52] M. Edstrand, "On the Crystal Structure of Antimony Oxychloride $Sb_4O_5Cl_2$ and Isomorphous Oxybromide," *Acta Chemica Scandinavica*, 178-203 (1947).

[53] C. Sarnstrand, "The Crystal Structure of Antimony (III) Chloride Oxide $Sb_4O_5Cl_2$," *Acta Crystallographica Section B: Structural Crystallography and Crystal Chemistry*, **34** 2402-2407 (1973).

[54] X. Su, Y. Liu, C. Xiao, G. Zhang, T. Liu, J. Qin, C. Chen, "A Facile, Clean and Quantitative Synthesis of Antimony Chloride Oxide Single Crystals." *Materials Letters,* **60**, 3879-3881 (2006).

[55] H. Katzke, Y. Oka, Y. Kanke. K. Kato and T. Yao, "Structure of Triantimony Tetraoxide Chloride, Sb_3O_4Cl: Twinning and One-Dimensional Disorder."*Zeitschrift für Kristallographie,* **214**, 284-289 (1999).

[56] Z. Mayerová, M. Johnsson and S. Lidin, "The Structure of Onoratoite, $Sb_8O_{11}X_2$ (X = Cl, Br) Revisited," *Solid state sciences,* **8**, 849-854 (2006).

[57] B. J. Li, Y. B. Zhao, X. M. Xu, H. Zhou, B. F. He, Z. S. Wu and Z. J. Zhang, *Ultraso. Sonochem.* **14**, 557 (2007).

[58] Z. Bo, M. Meihua and G. Jiansheng, Electrochemical Synthesis of $Sb_4O_5Cl_2$, *Chinese Journal of Applied Chemistry*, **24**, 226-228 (2007).

[59] X. Y. Chen, H. S. Huh and S. W. Lee, "Hydrothermal Synthesis of Antimony Oxychloride and Oxide Nanocrystals: $Sb_4O_5Cl_2$, $Sb_8O_{11}Cl_2$, and Sb_2O_3,"*Journal of Solid State Chemistry,* **181**, 2127-2132 (2008).

[60] J. J. Tang, Y. Wang, Z. Jiao and M. Wu, "Self-Assembly Nanostructures of One-Dimensional Antimony Oxide and Oxychloride," *Materials Letters,* **63**, 1481-1484 (2009).

[61] J. Zhou, H. Zhao, L. Li, M. Tian, J. Han, L. Zhang and L. Guo, "One-Step Synthesis and Flame Retardancy of Sheaf-Like Microcrystal Antimony Oxychloride, " *Journal of nanoscience and nanotechnology*, **11,** 8504-8509 (2011).

[62] Y. J. Zheng, H. Teng and M. Bai, *Journal of Central South University (Science and Technology*), **42**, 1549-1554, (2011).

[63] L. Yang, J. Huang, L. Cao, L. Shi, Q. Yu, X. Kong, Y. Jie, "pH-Regulated Template-Free Assembly of $Sb_4O_5Cl_2$ Hollow Microsphere Crystallites With Self -Narrowed Band Gap and Optimized Photocatalytic Performance," *Scientific Reports,* **6** 27765 (2016).

[64] P. Li, J. Shu, L. Shao, X. Lin, K. Wu, M. Shui, D. Wang, N. Long and Y. Ren, "Comparison of Morphology and Electrochemical Behavior between $PbSbO_2Cl$ and $PbCl_2/Sb_4O_5Cl_2$," *Journal of Electroanalytical Chemistry,* **731,** 128–132 (2014).

[65] Q. Jiang, X. Yuan, H. Wang, X. Chen, S. Gu, Y. Liu, Z. Wuab and G. Zengab, "A Facile Hydrothermal Method to Synthesize Sb_2S_3/ $Sb_4O_5Cl_2$ Composites with three-Dimensional Spherical Structures," *RSC Adv*, **5**, 53019–53024 (2015).

[66] V. V Bogdanova, S. S. Fedeev, A. I. Lesnikovich and V. V. Sviridov "The Formation of Antimony Oxychloride in Flame Retardant Mixture and its Influence on Flame Retardant Efficiency," *Polymer Degradation and Stability*, **11**, 205 (1985).

[67] H. Li, X. J. Huang and L. Q Chen. *Solid State Ionics*, **121**, 89–197 (1999).

[68] Q. Jiang, X. Yuan, H. Wang, X. Chen, S. Gu, Yang Liu, Z. Wu and G. Zeng, "A Facile Hydrothermal Method to Synthesize $Sb_2S_3/Sb_4O_5Cl_2$ Composites with Three-Dimensional Spherical Structures," *RSC Adv*., **5,** 53019–53024 (2015).

[69] A. Gupta, P. Singh, C. Shivakumara, "Synthesis of $BaSO_4$ Nanoparticles by Precipitation Method Using Sodium Hexa Metaphosphate as a Stabilizer," *Solid State Communications,* **150**, 386–388 (2010).

[70] T. Jose, S. C George, M. MG and S. Thomas, "Functionalized MWCNT and PVA Nanocomposite Membranes for Dielectric and Pervaporation Applications," *J Chem Eng Process Technol.*, **6**, 233-211 (2015).

[71] C. Lia, X. Yang, Y. Liu, Z. Zhao and Y. Qian, "Growth Of Crystalline Sb_2S_3 Nanorods By Hydrothermal Method," *Journal of Crystal Growth,* **255**, 342–347 (2003).

[72] L. V. Azároff and M J. Buerger. "The Powder Method in X-ray Crystallography," **342** (1953).

[73] B. D. Cullity, "Elements of X-Ray Diffraction," second ed., *Addison-Wesley Publishing Company*, (1978).

[74] G. K. Williamson, W. H. Hall, *Acta Metall,* **1**, (1958).

[75] N.S. Gonçalves, J.A. Carvalho, Z.M. Lima and J.M. Sasaki, "Size Strain Study of NiO Nanoparticles by X-Ray Powder Diffraction Line Broadening," *Materials Letters*, **72** 36–38 (2012).

[76] L. Wu, L. Zhang, Z. Xun, G. Yu, and L. Shi, "Effect of Growth Temperature and Time on Morphology and Gas Sensitivity of Cu_2O/Cu Microstructures," *Journal of Nanomaterials,* **2016**, 10 pages (2016).

[77] A. N. Bugrov and O. V. Almjasheva, "Effect of Hydrothermal Synthesis Conditions on the Morphology of ZrO_2 Nanoparticles," *Nanosystems: Physics, Chemistry, Mathematics,* 810-815 (2013).

[78] T. D Malevu, R. O Ocaya, "Effect of Annealing Temperature on Structural, Morphology and Optical Properties of ZnO Nano-Needles Prepared by Zinc Air Cell System Method," *Int. J. Electrochem. Sci*., **10** 1752–1761 (2015).

[79] A. Chandran, N. Francis, T. Jose and K. C. George, "Synthesis Structural Characterization and Optical Band Gap Determination of ZnS Nanoparticles," *Acad Rev*, **17**, 17-21 (2010).

[80] M. Ganguly, S. K. Rout, H. Y. Park, C. W. Ahn and I. W. Kim, "Structural, Dielectric and Optical Characterization of Cerium Doped Barium Titanate. "*Physics Express*, **3** 1-12 (2013).

[81] E. Roduner, "Size matters: why nanomaterials are different," *Chemical Society Reviews,* **35**,583-592 (2006)**.**

[82] Z. Z. Sheng and A. M. Hermann "Superconductivity in the Rare-Earth-

Free Tl Ba Cu O System above Liquid-Nitrogen Temperature," *Nature*, **332**. 55-58 (1988).

[83] A. M. Hermann and J. V. Yakhmi, "Thallium-Based High-Temperature," *Superconductors* (1994) (New York: Dekker).

[84] T. Kayed, "Properties of Boron Doped Tl–Ba–Ca–Cu–O Superconductors," *Materials Research Bulletin*, **38** 533-538 (2003).